Vlasov formalism for extended relativistic mean field models: The crust-core transition and the stellar matter equation of state

Helena Pais and Constança Providência
CFisUC, Department of Physics, University of Coimbra, 3004-516 Coimbra, Portugal
(Received 3 March 2016; revised manuscript received 27 May 2016; published 29 July 2016)

The Vlasov formalism is extended to relativistic mean field hadron models with nonlinear terms up to fourth order and applied to the calculation of the crust-core transition density. The effect of the nonlinear $\omega\rho$ and $\sigma\rho$ coupling terms on the crust-core transition density and pressure and on the macroscopic properties of some families of hadronic stars is investigated. For that purpose, six families of relativistic mean field models are considered. Within each family, the members differ in the symmetry energy behavior. For all the models, the dynamical spinodals are calculated, and the crust-core transition density and pressure and the neutron star mass-radius relations are obtained. The effect on the star radius of the inclusion of a pasta calculation in the inner crust is discussed. The set of six models that best satisfy terrestrial and observational constraints predicts a radius of 13.6 ± 0.3 km and a crust thickness of 1.36 ± 0.06 km for a $1.4M_{\odot}$ star.

DOI: 10.1103/PhysRevC.94.015808

I. INTRODUCTION

The dynamical response of nuclear matter in the collisionless, low-energy regime is adequately described within the Vlasov equation, a semiclassical approach that takes into account the correct particle statistics. It is a good approximation to the time-dependent Hartree–Fock equation at low energies [1] and was used to study heavy-ion collisions at low-intermediate energies [2–5]. In Refs. [6,7], the collective modes in cold and hot nuclear matter described with the Walecka model were successfully calculated within this formalism. An extension of the formalism was carried out, including nonlinear meson terms in the Lagrangian density [8–11] or density-dependent meson couplings [12]. It has also been shown to be a good tool to estimate the crust-core transition in cold neutrino-free neutron stars [13,14]. Similar calculations based on the Skyrme interaction had been developed previously [15]. In Refs. [13,14], different calculations of the transition density at several temperatures and isospin asymmetries were compared, and it was found that the dynamical spinodal method predicts a lower limit for the crust-core density, and that the larger the isospin asymmetry, the closer this value is to the Thomas–Fermi estimate. For β-equilibrium matter, i.e., neutron star matter, both results are very similar.

Unified equations of state (EoS), that is, EoS that describe the neutron star from its outer crust to the inner core within the same nuclear model, are generally not available. Consequently, the complete EoS is frequently built out of three different pieces: one for the outer crust, another for the inner crust, and one for the core, obtained from different models. Recently, it was shown in Ref. [16] that, although star properties such as mass and radius do not depend on the outer crust EoS, the choice of the inner crust EoS and the matching of the inner crust EoS to the core EoS may be critical, and variations larger than 0.5 km have been obtained for the radius of a $1.4M_{\odot}$ star.

For the outer crust, three EoS are used in the literature: the Baym–Pethick–Sutherland (BPS) EoS [17], the Haensel and Pichon (HP) EoS [18], or the Rüster *et al.* (RHS) EoS [19]. Essentially, the differences existing among them do not affect the mass-radius curves. This is no longer true for matter above the neutron drip line. The inner crust of neutron stars may contain exotic geometrical structures termed nuclear pasta [20] at its upper boarder, just before the crust-core transition. Several methods have been used to compute these pasta phases: quantum [21], semiclassical [22,23], or classical [24] molecular dynamics calculations, three-dimensional (3D) Hartree–Fock calculations [25,26], and Thomas–Fermi (TF) calculations [13,14,27–29]. The authors of Ref. [30] attribute to the existence of pasta phases a high-impurity parameter corresponding to a large resistivity that causes a very fast magnetic-field decay and explains the absence of isolated pulsars with periods above 12 s. In the present study, the complete stellar matter EoS will be constructed by taking (i) a standard EoS for the outer crust, such as BPS, HP, or RHS, (ii) an adequate inner crust EoS that matches the outer crust EoS at the neutron drip, and the core EoS at the crust-core transition, and (iii) the core EoS. After having the complete EoS, star properties such as the mass and radius are determined from the integration of the Tolman–Oppenheimer–Volkof equations [31,32].

Laboratory measurements and first-principle calculations put limits on the EoS that describe neutron stars. An example is the microscopic calculations based on nuclear interactions derived from chiral effective field theory [33], or on realistic two- and three-nucleon interactions, using quantum Monte Carlo (MC) techniques [34]. However, in these approaches there is a reasonable uncertainty associated with the three-body force, meaning that small differences between RMF models and MC results should not be enough to discard those models. Other constraints come from terrestrial experiments, like collective-flow data in heavy-ion collisions [35] and the KaoS experiment [36], or the measurement of saturation-density properties and properties of nuclei such as the binding energy and rms radii [37]. Observational constraints also play a fundamental role. In 2010 and 2013, two very massive pulsars, PSR J1614-2230 [38] and PSR J0348+0432 [39], respectively, both close to $M \sim 2M_{\odot}$, were observed. An

updated determination of the PSR J1614-2230 mass has reduced this value to $1.928 \pm 0.017 M_\odot$ [40]. Radii are still not sufficiently constrained, but European Space Agency (ESA) missions such as the Advanced Telescope for High-energy Astrophysics (Athena+) [41] and the Theia space mission will allow, among other things, to better constraint the M/R relation of neutron stars.

Appropriate nuclear models should satisfy both kinds of constraints: observational and terrestrial. The NL3 [42] parametrization has been fit to the ground-state properties of both stable and unstable nuclei. It is able to predict $2M_\odot$, but its symmetry energy slope is too large, and it is too hard at high densities. Other nucleonic EOS that satisfy the $2M_\odot$ constraint have been discussed in the literature; see, for instance, Refs. [43–45]. However, some nucleonic models agree well with the phenomenology at low and intermediate densities but fail to produce $2M_\odot$ stars because they predict a too-soft EoS. Introducing adequate new nonlinear terms in the Lagrangian density will change the density dependence of the EoS so as to correct its behavior either by inducing a softening [46–48] or hardening [49,50] of the EoS. Experimental results at intermediate densities are essential to constrain these terms.

The transition pressure plays a very important role in the determination of the fraction of the star moment of inertia contained in the crust [51]. The description of glitches considers that the inner crust is a reservoir of angular momentum and, in Ref. [51], the authors estimated that the observed glitches of Vela would be explained if 1.4% of the total momentum of inertia of the star resides in the crust. More recently, it was shown that crustal entrainment requires, in fact, a larger angular-momentum reservoir in the crust [52] associated with a fraction of the total momentum of inertia larger than that the crust may contain. Possible solutions to solve this problem include the contribution of the core to the glitch mechanism [53], or the choice of an appropriate EoS that predicts a sufficiently large pressure at the crust-core transition [54].

We analyze the effect of the $\sigma\rho$ and $\omega\rho$ couplings on the crust-core transition density and pressure at zero temperature, starting from three different relativistic mean field (RMF) models, TM1 [48], NL3 [42], and Z271 [46,47]. These three models will be designated as the *heads* of the families of the models that we are going to construct by adding the terms $\sigma\rho$ or $\omega\rho$ with different coupling strengths. Thus, in the following work, we are going to consider six different RMF families. While NL3 and TM1 have been fit to the ground-state properties of several nuclei, the symmetry energy slope that these models predict at saturation density is too high. Z271 with the NL3 saturation properties has a softer EoS at large densities due to the inclusion of a fourth-order term in ω. The first two predict neutron stars with masses above the constraints set by the pulsars J1614-2230 and J0348+0432, while the third fails to satisfy these constraints. However, in Ref. [55], it has been shown that Z271$\omega\rho$5 and Z271$\omega\rho$6 were two of the few models that passed a set of 11 terrestrial constraints. We consider several strengths of the couplings of the $\sigma\rho$ and $\omega\rho$ terms in order to generate a set of models that span the values of the symmetry energy and its slope at saturation as obtained in different experiments [37]. It will be possible to identify existing correlations between the slope L and the density and pressure transitions in a systematic way, since in each family the isoscalar properties are kept fixed and only the isovector properties change. We then select, from among the six families, the models that satisfy a set of well-accepted saturation properties and constraints from microscopic calculations and still produce a star with mass larger than $2M_\odot$. Since the Z271 family does not satisfy the latter constraint, we implement the mechanism proposed in Ref. [50]; adding an extra nonlinear σ function that hardens the EoS above saturation.

One of the objectives of the work is to distinguish the effect of the terms of the form $\omega\rho$ and $\sigma\rho$ when modifying the density dependence of the symmetry energy. We consider terms of the form $f_i^2\rho^2$, with $f_i = \omega$ or σ, as in Refs. [46,47], which will affect the neutron skin thickness of nuclei but do not change some well-established properties of nuclei, such as the binding energy and the charge radius. In Ref. [56], where a nonlinear $\sigma\rho$ term of the form $\sigma\rho^2$ was used, and a refitting of other parameters kept the binding energy and the charge radius unchanged, a nonlinear behavior of the transition density with L was obtained, in contrast to previous studies [57,58]. We will also pay special attention to the effect of these terms on the pressure at the crust-core transition, since this is a quantity that directly shows whether the glitch mechanism could be attributed solely to the crust.

To calculate the crust-core transition properties, we extend the Vlasov formalism previously used to include all nonlinear self-interaction and mixing terms involving the σ, ω, and ρ mesons up to fourth order. Taking the six families of models described above, we determine the crust-core transition density and pressure and discuss possible implications of the different density dependence of the symmetry energy on the properties of neutron stars, especially the effects on the star radius.

In Sec. II, we present the formalism and derive the dispersion relation within the Vlasov method for the calculation of the dynamical spinodal with the nonlinear σ, ω, and ρ meson coupling terms. In Sec. III, the formalism is applied to the determination of the crust-core transition, and the construction of a consistent stellar matter EoS, and, finally, in Sec. IV, a few conclusions are drawn.

II. FORMALISM

We use the relativistic nonlinear Walecka model (NLWM) in the mean field approximation, within the Vlasov formalism to study nuclear collective modes of asymmetric nuclear matter and *npe* matter at zero temperature [6,7]. We first review the Lagrangian density of the extended RMF model with all meson terms up to quartic order [59,60], and we next present the Vlasov formalism to study the collective model of nuclear matter.

A. Extended relativistic mean field Lagrangian

We consider a system of baryons with mass M interacting with and through an isoscalar-scalar field ϕ with mass m_s, an isoscalar-vector field V^μ with mass m_v, and an isovector-vector field $\mathbf{b}^\mu$ with mass m_ρ. When describing *npe* matter, we also include a system of electrons with mass m_e. Protons

and electrons interact through the electromagnetic field A^μ. The Lagrangian density reads

$$\mathcal{L} = \sum_{i=p,n} \mathcal{L}_i + \mathcal{L}_e + \mathcal{L}_\sigma + \mathcal{L}_\omega + \mathcal{L}_\rho + \mathcal{L}_{\sigma\omega\rho} + \mathcal{L}_A,$$

where the nucleon Lagrangian reads

$$\mathcal{L}_i = \bar{\psi}_i[\gamma_\mu i D^\mu - M^*]\psi_i,$$

with

$$i D^\mu = i\partial^\mu - g_v V^\mu - \frac{g_\rho}{2}\boldsymbol{\tau}\cdot\mathbf{b}^\mu - eA^\mu\frac{1+\tau_3}{2},$$
$$M^* = M - g_s\phi,$$

and the electron Lagrangian is given by

$$\mathcal{L}_e = \bar{\psi}_e[\gamma_\mu(i\partial^\mu + eA^\mu) - m_e]\psi_e.$$

The isoscalar part is associated with the scalar sigma (σ) field ϕ and the vector omega (ω) field V_μ, whereas the isospin dependence comes from the isovector-vector rho (ρ) field b^i_μ (where μ stands for the four-dimensional spacetime indices and i is the three-dimensional isospin direction index). The associated Lagrangians are

$$\mathcal{L}_\sigma = +\frac{1}{2}\left(\partial_\mu\phi\partial^\mu\phi - m_s^2\phi^2 - \frac{1}{3}\kappa\phi^3 - \frac{1}{12}\lambda\phi^4\right),$$
$$\mathcal{L}_\omega = -\frac{1}{4}\Omega_{\mu\nu}\Omega^{\mu\nu} + \frac{1}{2}m_v^2 V_\mu V^\mu + \frac{1}{4!}\xi g_v^4\left(V_\mu V^\mu\right)^2,$$
$$\mathcal{L}_\rho = -\frac{1}{4}\mathbf{B}_{\mu\nu}\cdot\mathbf{B}^{\mu\nu} + \frac{1}{2}m_\rho^2\mathbf{b}_\mu\cdot\mathbf{b}^\mu,$$
$$\mathcal{L}_A = -\frac{1}{4}F_{\mu\nu}F^{\mu\nu}, \tag{1}$$

where $\Omega_{\mu\nu} = \partial_\mu V_\nu - \partial_\nu V_\mu$, $\mathbf{B}_{\mu\nu} = \partial_\mu\mathbf{b}_\nu - \partial_\nu\mathbf{b}_\mu - g_\rho(\mathbf{b}_\mu\times\mathbf{b}_\nu)$, and $F_{\mu\nu} = \partial_\mu A_\nu - \partial_\nu A_\mu$. We supplement the meson Lagrangian with all the nonlinear terms that mix the σ, ω, and ρ mesons up to quartic order [59–62],

$$\begin{aligned}\mathcal{L}_{\sigma\omega\rho} = {}& \Lambda_{3\sigma} g_s g_v^2\phi V_\mu V^\mu + \Lambda_{2\sigma} g_s^2 g_v^2\phi^2 V_\mu V^\mu \\ & + \Lambda_{1\sigma} g_s g_\rho^2\phi\mathbf{b}_\mu\cdot\mathbf{b}^\mu + \Lambda_\sigma g_s^2 g_\rho^2\phi^2\mathbf{b}_\mu\cdot\mathbf{b}^\mu \\ & + \Lambda_\omega g_v^2 g_\rho^2\mathbf{b}_\mu\cdot\mathbf{b}^\mu V_\mu V^\mu.\end{aligned} \tag{2}$$

An adequate choice of the parameters of the model will allow us to build parametrizations compatible with both laboratory measurements and astrophysical observations [61,62]. The model comprises the following parameters: three coupling constants g_s, g_v, and g_ρ of the mesons to the nucleons, the bare nucleon mass M, the electron mass m_e, the masses of the mesons, the electromagnetic coupling constant, $e = \sqrt{4\pi/137}$, the self-interacting coupling constants, κ, λ, and ξ, and the mixing self-interacting coupling constants, Λ_ω, Λ_σ, $\Lambda_{i\sigma}$, $i = 1,2,3$. In this Lagrangian density, $\boldsymbol{\tau}$ are the Pauli matrices.

B. The Vlasov formalism

In the sequel we use the formalism developed in Refs. [6,7], where the collective modes in cold nuclear matter were determined within the Vlasov formalism based on the Walecka model [63]. In the present section, we extend the Vlasov formalism and include all meson terms up to quartic order. We use, whenever possible, the notation introduced in Refs. [6,7].

The time evolution of the distribution functions f_i is described by the Vlasov equation

$$\frac{\partial f_i}{\partial t} + \{f_i, h_i\} = 0, \quad i = p, n, e, \tag{3}$$

where $\{,\}$ denotes the Poisson brackets. The Vlasov equation expresses conservation of the number of particles in phase space and is, therefore, covariant.

The state that minimizes the energy of asymmetric nuclear matter is characterized by the Fermi momenta P_{Fi}, $i = p,n$, $P_{Fe} = P_{Fp}$ and is described by the equilibrium distribution function at zero temperature:

$$f_0(\boldsymbol{r},\boldsymbol{p}) = \mathrm{diag}\left[\Theta\left(P_{Fp}^2 - p^2\right), \Theta\left(P_{Fn}^2 - p^2\right), \Theta\left(P_{Fe}^2 - p^2\right)\right] \tag{4}$$

and by the constant mesonic fields, which obey the following equations:

$$\begin{aligned} m_s^2\phi_0 + \frac{\kappa}{2}\phi_0^2 + \frac{\lambda}{6}\phi_0^3 - 2\Lambda_\sigma g_\sigma^2 g_\rho^2\phi_0 b_0^{(0)2} - \Lambda_{1\sigma} g_\sigma g_\rho^2 b_0^{(0)2} - 2\Lambda_{2\sigma} g_\sigma^2 g_v^2\phi_0 V_0^{(0)2} - \Lambda_{3\sigma} g_\sigma g_v^2 V_0^{(0)2} &= g_s\rho_s^{(0)}, \\ m_v^2 V_0^{(0)} + \frac{1}{6}\xi g_v^4 V_0^{(0)3} + 2\Lambda_\omega g_v^2 g_\rho^2 V_0^{(0)} b_0^{(0)2} + 2\Lambda_{2\sigma} g_v^2 g_\sigma^2 V_0^{(0)}\phi_0^2 + 2\Lambda_{3\sigma} g_v^2 g_\sigma V_0^{(0)}\phi_0 &= g_v j_0^{(0)}, \\ m_\rho^2 b_0^{(0)} + 2\Lambda_\omega g_\rho^2 g_v^2 V_0^{(0)2} b_0^{(0)} + 2\Lambda_\sigma g_\rho^2 g_\sigma^2\phi_0^2 b_0^{(0)} + 2\Lambda_{1\sigma} g_\rho^2 g_\sigma\phi_0 b_0^{(0)} &= \frac{g_\rho}{2} j_{3,0}^{(0)}, \\ V_i^{(0)} = b_i^{(0)} = A_0^{(0)} = A_i^{(0)} &= 0, \end{aligned} \tag{5}$$

where $\rho_s^{(0)}$, $j_0^{(0)}$, $j_{3,0}^{(0)}$ are, respectively, the equilibrium scalar density, the nuclear density, and the isospin density.

Collective modes in the present approach correspond to small oscillations around the equilibrium state. These small deviations are described by the linearized equations of motion and collective modes are given as solutions of those equations. To construct them, let us define:

$$f_i = f_{0i}^{(0)} + \delta f_i, \quad \phi = \phi_0 + \delta\phi, \quad V_0 = V_0^{(0)} + \delta V_0,$$
$$V_i = \delta V_i, \quad b_0 = b_0^{(0)} + \delta b_0, \quad b_i = \delta b_i,$$
$$A_0 = \delta A_0, \quad A_i = \delta A_i.$$

As in Refs. [6–8,64], we express the fluctuations of the distribution functions in terms of the generating functions:

$$S(\mathbf{r},\mathbf{p},t) = \mathrm{diag}(S_p, S_n, S_e),$$

such that

$$\delta f_i = \{S_i, f_{0i}\} = -\{S_i, p^2\}\delta\big(P_{Fi}^2 - p^2\big).$$

The linearized Vlasov equations for δf_i,

$$\frac{d\delta f_i}{dt} + \{\delta f_i, h_{0i}\} + \{f_{0i}, \delta h_i\} = 0,$$

are equivalent to the following time-evolution equations:

$$\frac{\partial S_i}{\partial t} + \{S_i, h_{0i}\} = \delta h_i = -g_s\frac{M^*}{\epsilon_0}\delta\phi - \frac{\mathbf{p}\cdot\delta\boldsymbol{\mathcal{V}}_i}{\epsilon_0} + \delta\mathcal{V}_{0i}, \quad i = p,n, \tag{6}$$

$$\frac{\partial S_e}{\partial t} + \{S_e, h_{0e}\} = \delta h_e = -e\left[\delta A_0 - \frac{\mathbf{p}\cdot\delta\mathbf{A}}{\epsilon_{0e}}\right], \tag{7}$$

where

$$\delta\mathcal{V}_{0i} = g_v\delta V_0 + \tau_i\frac{g_\rho}{2}\delta b_0 + e\frac{1+\tau_i}{2}\delta A_0,$$

$$\delta\boldsymbol{\mathcal{V}}_i = g_v\delta\mathbf{V} + \tau_i\frac{g_\rho}{2}\delta\mathbf{b} + e\frac{1+\tau_i}{2}\delta\mathbf{A},$$

$$h_{0i} = \epsilon_0 + \mathcal{V}_{0i}^{(0)} = \sqrt{p^2 + M^{*2}} + \mathcal{V}_{0i}^{(0)}$$

$$h_{0e} = \epsilon_{0e} = \sqrt{p^2 + m_e^2}.$$

which has only to be satisfied for $p = P_{Fi}$.

Of particular interest on account of their physical relevance are the longitudinal modes, with wave vector $\mathbf{k}$ and frequency ω, described by the ansatz

$$\begin{pmatrix} S_j(\mathbf{r},\mathbf{p},t) \\ \delta\phi \\ \delta\zeta_0 \\ \delta\zeta_i \end{pmatrix} = \begin{pmatrix} \mathcal{S}_\omega^j(\cos\theta) \\ \delta\phi_\omega \\ \delta\zeta_\omega^0 \\ \delta\zeta_\omega^i \end{pmatrix} e^{i(\omega t - \mathbf{k}\cdot\mathbf{r})}, \tag{8}$$

where $j = p,n,e$, $\zeta = V,b,A$ represent the vector-meson fields, and θ is the angle between $\mathbf{p}$ and $\mathbf{k}$. The wave vector of the excitation mode, $\mathbf{k}$, is identified with the momentum transferred to the system through the process which gives rise to the excitation.

For the longitudinal modes, we get $\delta V_\omega^x = \delta V_\omega^y = 0$, $\delta b_\omega^x = \delta b_\omega^y = 0$, and $\delta A_\omega^x = \delta A_\omega^y = 0$. Calling $\delta V_\omega^z = \delta V_\omega$, $\delta b_\omega^z = \delta b_\omega$, and $\delta A_\omega^z = \delta A_\omega$, we have for the fields $\delta\mathcal{V}_{i,z} = \delta\mathcal{V}_\omega^i e^{i(\omega t - \mathbf{k}\cdot\mathbf{r})}$ and $\delta\mathcal{V}_{0i} = \delta\mathcal{V}_\omega^{0i} e^{i(\omega t - \mathbf{k}\cdot\mathbf{r})}$. Replacing the ansatz (8) in Eqs. (6) and (7), we get

$$i(\omega - \omega_{0i}x)\mathcal{S}_\omega^i = -g_s\frac{M^*}{\epsilon_{Fi}}\delta\phi_\omega - V_{Fi}x\delta\mathcal{V}_\omega^i, \tag{9}$$

$$i(\omega - \omega_{0e}x)\mathcal{S}_\omega^e = -e\delta A_\omega^0 + eV_{Fe}x\delta A_\omega, \tag{10}$$

$$\big(\omega^2 - k^2 - m_{s,\mathrm{eff}}^2\big)\delta\phi_\omega = -\chi_1\delta b_\omega^0 - \chi_2\delta V_\omega^0 - \frac{2ig_sM^*}{(2\pi^2)}\sum_{i=p,n}P_{Fi}\omega_{0i}\int_{-1}^{1}xS_\omega^i(x)dx, \tag{11}$$

$$\big(\omega^2 - k^2 - m_{v,\mathrm{eff}}^2\big)\delta V_\omega^0 = \chi_v\delta b_\omega^0 + \chi_2\delta\phi_\omega - \frac{2ig_v}{(2\pi^2)}\sum_{i=p,n}\omega_{0i}P_{Fi}\epsilon_{Fi}\int_{-1}^{1}xS_\omega^i(x)dx, \tag{12}$$

$$\big(\omega^2 - k^2 - m_{\rho,\mathrm{eff}}^2\big)\delta b_\omega^0 = \chi_v\delta V_\omega^0 + \chi_1\delta\phi_\omega - \frac{ig_\rho}{(2\pi^2)}\sum_{i=p,n}\tau_i\omega_{0i}P_{Fi}\epsilon_{Fi}\int_{-1}^{1}xS_\omega^i(x)dx, \tag{13}$$

$$(\omega^2 - k^2)\delta A_\omega^0 = -\frac{2ei}{(2\pi^2)}\sum_{i=p,e}\omega_{0i}P_{Fi}\epsilon_{Fi}\int_{-1}^{1}x\big[S_\omega^p(x) - S_\omega^e(x)\big]dx, \tag{14}$$

with $x = \cos\theta$, $i = p,n$, $\omega_{0j} = kV_{Fj} = kP_{Fj}/\epsilon_{Fj}$, $j = p,n,e$, $\chi_v = 4\Lambda_\omega g_v^2 g_\rho^2 V_0^{(0)} b_0^{(0)}$, $\chi_1 = 4\Lambda_\sigma g_\sigma^2 g_\rho^2\phi_0 b_0^{(0)} + 2\Lambda_{1\sigma}g_\sigma g_\rho^2 b_0^{(0)}$, $\chi_2 = 4\Lambda_{2\sigma}g_\sigma^2 g_v^2\phi_0 V_0^{(0)} + 2\Lambda_{3\sigma}g_\sigma g_v^2 V_0^{(0)}$, and

$$\begin{aligned} m_{s,\mathrm{eff}}^2 &= m_s^2 + \kappa\phi_0 + \lambda/2\phi_0^2 - 2\Lambda_\sigma g_\sigma^2 g_\rho^2 b_0^{(0)2} - 2\Lambda_{2\sigma}g_\sigma^2 g_v^2 V_0^{(0)2} + g_s^2\frac{d\rho_s^0}{dM^*}, \\ m_{v,\mathrm{eff}}^2 &= m_v^2 + \frac{1}{2}g_v^4\xi V_0^{(0)2} + 2\Lambda_\omega g_v^2 g_\rho^2 b_0^{(0)2} + 2\Lambda_{2\sigma}g_\sigma^2 g_v^2\phi_0^2 + 2\Lambda_{3\sigma}g_\sigma g_v^2\phi_0, \\ m_{\rho,\mathrm{eff}}^2 &= m_\rho^2 + 2\Lambda_\omega g_\rho^2 g_v^2 V_0^{(0)2} + 2\Lambda_\sigma g_\sigma^2 g_\rho^2\phi_0^2 + 2\Lambda_{1\sigma}g_\sigma g_\rho^2\phi_0, \end{aligned} \tag{15}$$

and from the continuity equation for the density currents, we get for the components of the vector fields

$$k\delta V_\omega = \omega\frac{B_v}{B_{v_1}}\delta V_\omega^0 - \frac{\omega}{B_{v_1}}\big(\chi_v\delta b_\omega^0 + \chi_2\delta\phi_\omega\big), \tag{16}$$

$$k\delta b_\omega = \omega\delta b_\omega^0 - \frac{\omega}{B_\rho}\big(\chi_v\delta V_\omega^0 + \chi_1\delta\phi_\omega\big), \tag{17}$$

$$k\delta A_\omega = \omega\delta A_\omega^0. \tag{18}$$

with $B_v = \omega^2 - k^2 - m^2_{v,\mathrm{eff}}$, $B_{v_1} = \omega^2 - k^2 - m^2_{v,\mathrm{eff},1}$, $B_\rho = \omega^2 - k^2 - m^2_{\rho,\mathrm{eff}}$, and $m^2_{v,\mathrm{eff},1} = m_v^2 + \frac{1}{6} g_v^4 \xi V_0^{(0)2} + 2\Lambda_\omega g_v^2 g_\rho^2 b_0^{(0)2} + 2\Lambda_{2\sigma} g_\sigma^2 g_v^2 \phi_0^2 + 2\Lambda_{3\sigma} g_\sigma g_v^2 \phi_0$.

The solutions of Eqs. (9)–(14) form a complete set of eigenmodes that may be used to construct a general solution for an arbitrary longitudinal perturbation. Substituting the set of equations (11)–(14) into Eqs. (9) and (10), we get a set of equations for the unknowns $\mathcal{S}^i_\omega$, which lead to the following matrix equation:

$$\begin{pmatrix} 1 + F^{pp} L_p & F^{pn} L_p & C_A^{pe} L_p \\ F^{np} L_n & 1 + F^{nn} L_n & 0 \\ C_A^{ep} L_e & 0 & 1 - C_A^{ee} L_e \end{pmatrix} \begin{pmatrix} A_{\omega p} \\ A_{\omega n} \\ A_{\omega e} \end{pmatrix} = 0, \tag{19}$$

with $A_{\omega i} = \int_{-1}^{1} x S_{\omega i}(x) dx$, $L_i = L(s_i) = 2 - s_i \ln((s_i+1)/(s_i-1))$, where $s_i = \omega/\omega_{0i}$, $F^{ij} = C_s^{ij} - C_v^{ij} - C_\rho^{ij} - C_A^{ij}\delta_{ip}\delta_{ij}$, and

$$C_A^{ij} = -\frac{e^2}{2\pi^2} \frac{1}{k^2} \frac{P_F^{j2}}{V_F^i}.$$

The coefficients C_s^{ij}, C_v^{ij}, and C_ρ^{ij} are given by

$$C_s^{ij} = \left[1 - \frac{\omega^2}{k^2}\left(\frac{g_v \chi_2}{B_{v_1}} + \frac{g_\rho \tau_i \chi_1}{2B_\rho}\right)\right] \frac{g_\sigma M^*}{2\pi^2 P_{F_i}} \left(f_\sigma^\sigma g_\sigma M^* P_{F_j} V_{F_j} + f_b^\sigma \frac{g_\rho}{2} \tau_j P_{F_j}^2 + f_\omega^\sigma g_v P_{F_j}^2\right), \tag{20}$$

$$C_v^{ij} = \left[1 - \frac{\omega^2}{k^2}\left(\frac{B_v}{B_{v_1}} - \frac{g_\rho \tau_i \chi_v}{2 g_v B_\rho}\right)\right] \frac{g_v}{2\pi^2 V_{F_i}} \left(f_\sigma^\omega g_\sigma M^* P_{F_j} V_{F_j} + f_b^\omega \frac{g_\rho}{2} \tau_j P_{F_j}^2 + f_\omega^\omega g_v P_{F_j}^2\right), \tag{21}$$

$$C_\rho^{ij} = \left[1 - \frac{\omega^2}{k^2}\left(1 - \frac{2 g_v \chi_v}{g_\rho \tau_i B_{v_1}}\right)\right] \frac{g_\rho \tau_i}{4\pi^2 V_{F_i}} \left(f_\sigma^b g_\sigma M^* P_{F_j} V_{F_j} + f_b^b \frac{g_\rho}{2} \tau_j P_{F_j}^2 + f_\omega^b g_v P_{F_j}^2\right). \tag{22}$$

The coefficients f_i^j read

$$f_\sigma^\sigma = \frac{1}{S}, \quad f_b^\sigma = -f_\sigma^\sigma \left(\frac{\chi_1 \chi_v^2}{B_\rho D_v} + \frac{\chi_1}{B_\rho} + \frac{\chi_2 \chi_v}{D_v}\right), \quad f_\omega^\sigma = -f_\sigma^\sigma \left(\frac{\chi_2 \chi_v^2}{B_v D_v} + \frac{\chi_2}{B_v} + \frac{\chi_1 \chi_v}{D_v}\right), \tag{23}$$

$$f_\sigma^\omega = f_\sigma^\sigma \frac{B_\rho}{D_v}\left(\frac{\chi_1 \chi_v}{B_\rho} + \chi_2\right), \quad f_b^\omega = S f_\sigma^\omega f_b^\sigma + \frac{\chi_v}{D_v}, \quad f_\omega^\omega = S f_\sigma^\omega f_\omega^\sigma + \frac{B_\rho}{D_v}, \tag{24}$$

$$f_\sigma^b = f_\sigma^\sigma \frac{B_v}{D_v}\left(\frac{\chi_2 \chi_v}{B_v} + \chi_1\right), \quad f_b^b = S f_\sigma^b f_b^\sigma + \frac{B_v}{D_v}, \quad f_\omega^b = S f_\sigma^b f_\omega^\sigma + \frac{\chi_v}{D_v}, \tag{25}$$

with $D_v = B_v B_\rho - \chi_v^2$, $S = B_\sigma + \frac{\chi_1^2}{B_\rho} + \frac{\chi_2^2}{B_v} + \frac{\chi_1^2 \chi_v^2}{D_v B_\rho} + \frac{\chi_2^2 \chi_v^2}{D_v B_v} + 2\frac{\chi_1 \chi_2 \chi_v}{D_v}$, and $B_\sigma = \omega^2 - k^2 - m^2_{s,\mathrm{eff}}$.

From Eq. (19), we get the following dispersion relation:

$$0 = \left(1 - C_A^{ee} L_e\right)[1 + F^{pp} L_p + F^{nn} L_n + (F^{pp} F^{nn} - F^{pn} F^{np}) L_p L_n] - C_A^{ep} C_A^{pe} L_p L_e (1 + F^{nn} L_n). \tag{26}$$

The density fluctuations are given by

$$\delta\rho_i = \frac{3}{2} \frac{k}{P_{Fi}} \rho_{0i} A_{\omega i}.$$

At subsaturation densities, there are unstable modes identified by the sign of the imaginary frequencies. For these modes, we define the growth rate $\Gamma = -i\omega$. The region in (ρ_p, ρ_n) space, for a given wave vector $\mathbf{k}$ and temperature T, limited by the surface $\omega = 0$, defines the dynamical spinodal surface. In the limit of $k = 0$ MeV, we recover the thermodynamic spinodal, which is defined by the surface in the (ρ_p, ρ_n, T) space for which the curvature matrix of the free-energy density is zero, i.e., has a zero eigenvalue. This relation has been discussed in Ref. [65].

III. RESULTS

In the present section, we discuss the effect of the two mixing terms $\omega\rho$ and $\sigma\rho$ on the crust-core transition properties and the importance of using an unified inner-crust-core EoS in the determination of the star radius. Starting from the RMF models NL3 [42], TM1 [66], and Z271 [46], we build six families of models; each one having the same isoscalar properties, but varying the isovector properties through the mixed nonlinear terms $\omega\rho$ and $\sigma\rho$ (see Sec. III A). The properties of the models will be compared with present terrestrial and observational constraints and, for each family, the model(s) that satisfy these constraints will be identified. Next, we calculate the crust-core transition density and pressure for all the models by applying the Vlasov formalism; see Sec. III B. Taking the two NL3

TABLE I. Symmetric nuclear matter properties at saturation density ρ_0 for the $\sigma\rho$ models. For TM1, the binding energy per nucleon, E/A, is -16.26 MeV, the incompressibility coefficient K is 280 MeV, and the nuclear saturation density is 0.145 fm^{-3}. For NL3 and Z271, these values are, respectively, -16.24 MeV, 270/269 MeV, and 0.148 fm^{-3}. ρ_t and P_t are the crust-core transition density and pressure, respectively, for β-equilibrium *pne* matter at $T = 0$ MeV. P_N is the pressure for neutron matter at $\rho = \rho_0$. The values of the total binding energy per particle (B/A), charge radii (r_c), neutron radii (r_n), and $\Delta r_{\rm np}$ for ^{208}Pb, are also shown.

Model	Λ_σ	$E_{\rm sym}$ (MeV)	L (MeV)	$K_{\rm sym}$ (MeV)	K_τ (MeV)	ρ_t (fm^{-3})	P_t (MeV/fm^3)	P_N (MeV/fm^3)	B/A (MeV)	r_c (fm)	r_n (fm)	$\Delta r_{\rm np}$ (fm)
NL3	0	37.34	118	101	−696	0.055	0.258	5.978	−7.878	5.518	5.740	0.280
$\sigma\rho1$	0.004	35.85	99	4	−666	0.058	0.303	5.108	−7.891	5.519	5.723	0.262
$\sigma\rho2$	0.0072	34.88	88	−29	−620	0.063	0.365	4.546	−7.897	5.521	5.711	0.249
$\sigma\rho3$	0.011	33.85	76	−38	−553	0.069	0.408	4.004	−7.903	5.523	5.698	0.233
$\sigma\rho4$	0.0145	33	68	−28	−487	0.074	0.468	3.60	−7.908	5.526	5.686	0.218
$\sigma\rho5$	0.018	32.25	61	−6	−421	0.078	0.454	3.282	−7.911	5.530	5.675	0.203
$\sigma\rho6$	0.022	31.47	55	24	−348	0.081	0.382	2.991	−7.913	5.535	5.662	0.185
TM1	0	36.84	111	34	−517	0.060	0.328	5.479	−7.877	5.541	5.753	0.270
$\sigma\rho1$	0.004	34.99	94	−29	−499	0.064	0.360	4.724	−7.905	5.544	5.737	0.251
$\sigma\rho2$	0.0073	34.22	85	−56	−478	0.068	0.407	4.268	−7.910	5.545	5.727	0.239
$\sigma\rho3$	0.011	33.42	76	−67	−443	0.072	0.447	3.829	−7.915	5.548	5.716	0.226
$\sigma\rho4$	0.0146	32.72	68	−64	−403	0.076	0.458	3.469	−7.918	5.551	5.706	0.213
$\sigma\rho5$	0.019	31.93	60	−50	−350	0.079	0.427	3.104	−7.922	5.555	5.694	0.197
$\sigma\rho6$	0.022	31.43	56	−35	−313	0.080	0.379	2.896	−7.923	5.558	5.686	0.186
Z271	0	35.81	99	−16	−340	0.068	0.405	4.952	−7.777	5.519	5.702	0.241
$\sigma\rho1$	0.01	34.87	87	−65	−350	0.072	0.448	4.370	−7.784	5.521	5.691	0.229
$\sigma\rho2$	0.02	34.00	77	−92	−344	0.076	0.474	3.850	−7.791	5.522	5.680	0.216
$\sigma\rho3$	0.03	33.21	68	−104	−327	0.079	0.477	3.399	−7.797	5.524	5.670	0.203
$\sigma\rho4$	0.04	32.47	60	−106	−304	0.081	0.451	3.015	−7.802	5.527	5.659	0.191
$\sigma\rho5$	0.05	31.79	53	−100	−276	0.083	0.398	2.691	−7.806	5.530	5.649	0.177
$\sigma\rho6$	0.06	31.15	48	−88	−245	0.085	0.323	2.418	−7.810	5.533	5.639	0.164

families, we discuss the matching of the crust to the core to get the stellar matter EoS in Sec. III C. For the inner crust, several possibilities will be considered. Finally, we apply the conclusions of Sec. III C to construct the stellar matter EoS for the TM1 and Z271 families in Sec. III D, and we propose a set of procedures to build the stellar matter EoS from the knowledge of the crust-core density transition and the core EoS.

A. Equation of state

From all the terms presented in Eq. (2), we restrict our discussion to a set of models that have only one of the following two nonlinear coupling terms:

$$\mathcal{L}_{\omega\rho} = \Lambda_\omega g_v^2 g_\rho^2 V_\mu V^\mu \mathbf{b}_\mu \cdot \mathbf{b}^\mu, \tag{27}$$

$$\mathcal{L}_{\sigma\rho} = \Lambda_\sigma g_\sigma^2 g_\rho^2 \phi^2 \mathbf{b}_\mu \cdot \mathbf{b}^\mu, \tag{28}$$

to allow the modification of the density dependence of the symmetry energy by changing the ρ-meson effective mass [47] and discuss the star properties for different density dependencies of the symmetry energy. The models NL3$\omega\rho$, Z271$\omega\rho$, and Z271$\sigma\rho$ were taken from Ref. [47]. The others; namely, NL3$\sigma\rho$, TM1$\omega\rho$, and TM1$\sigma\rho$, are obtained by varying either the Λ_ω or Λ_σ coupling constants and by calculating the new g_ρ constants, so that the symmetry energy at $\rho = 0.1$ fm^{-3} has the same value as the reference model of the family.

Tables I and II show the nuclear matter properties at the saturation density for the models considered: the symmetry energy $\mathcal{E}_{\rm sym}$, the symmetry energy slope L, the symmetry energy curvature $K_{\rm sym}$, and $K_\tau = K_{\rm sym} - 6L - \frac{Q_0}{K}L$ (see Ref. [67]). The tables also show the crust-core transition density ρ_t and pressure P_t calculated from the Vlasov method, as will be shown in the next section, and the neutron matter pressure P_N calculated at the nuclear saturation density. Finally, the total binding energy per particle, the charge radii, the neutron radii, and the neutron skin thickness $\Delta r_{\rm np}$ for the ^{208}Pb nucleus are also given. We observe that the nonlinear $\omega\rho$ and $\sigma\rho$ terms do not change the binding energy of the nuclei or the charge radius in more than 1%. Our results agree well with those of Refs. [46,47]. The neutron radius and, therefore, the neutron skin thickness, decrease with decreasing L for both families.

In Fig. 1, we show the EoS of pure neutron matter for a set of models from Tables I and II and compare them with the result of microscopic calculations based on nuclear interactions derived from chiral effective field theory (EFT) [33], or on realistic two- and three-nucleon interactions, by using quantum

TABLE II. The same as in Table I but for the $\omega\rho$ models.

Model	Λ_ω	$E_{\rm sym}$ (MeV)	L (MeV)	$K_{\rm sym}$ (MeV)	K_τ (MeV)	ρ_t (fm^{-3})	P_t (MeV/fm^3)	P_N (MeV/fm^3)	B/A (MeV)	r_c (fm)	r_n (fm)	$\Delta r_{\rm np}$ (fm)
NL3	0	37.34	118	100	−696	0.055	0.258	5.978	−7.878	5.518	5.740	0.280
$\omega\rho1$	0.005	36.01	101	1	−680	0.057	0.291	5.146	−7.891	5.518	5.725	0.265
$\omega\rho2$	0.01	34.94	88	−46	−636	0.062	0.355	4.511	−7.899	5.519	5.712	0.251
$\omega\rho3$	0.015	33.98	77	−60	−578	0.068	0.437	3.998	−7.906	5.521	5.700	0.237
$\omega\rho4$	0.02	33.12	68	−53	−512	0.074	0.503	3.573	−7.912	5.524	5.688	0.223
$\omega\rho5$	0.025	32.36	61	−34	−445	0.080	0.533	3.213	−7.917	5.526	5.677	0.209
$\omega\rho6$	0.03	31.66	55	−8	−380	0.084	0.516	2.906	−7.921	5.530	5.667	0.195
TM1	0	36.84	111	33	−517	0.060	0.328	5.479	−7.877	5.541	5.753	0.270
$\omega\rho1$	0.005	35.12	95	−34	−511	0.063	0.350	4.760	−7.886	5.542	5.741	0.257
$\omega\rho2$	0.01	34.29	85	−73	−496	0.066	0.397	4.265	−7.872	5.542	5.733	0.249
$\omega\rho3$	0.015	33.54	76	−91	−468	0.071	0.455	3.845	−7.857	5.543	5.724	0.239
$\omega\rho4$	0.02	32.84	68	−94	−432	0.075	0.495	3.484	−7.828	5.545	5.715	0.228
$\omega\rho5$	0.025	32.20	61	−86	−392	0.079	0.510	3.167	−7.817	5.548	5.703	0.213
$\omega\rho6$	0.03	31.61	56	−72	−350	0.082	0.497	2.885	−7.791	5.552	5.689	0.195
Z271	0	35.81	99	−16	−340	0.068	0.405	4.952	−7.777	5.519	5.702	0.241
$\omega\rho1$	0.01	35.25	91	−66	−364	0.071	0.436	4.574	−7.783	5.519	5.696	0.234
$\omega\rho2$	0.02	34.72	83	−104	−379	0.072	0.454	4.245	−7.788	5.519	5.689	0.228
$\omega\rho3$	0.025	34.46	80	−120	−383	0.073	0.473	4.095	−7.791	5.520	5.686	0.225
$\omega\rho4$	0.03	34.21	77	−133	−386	0.074	0.483	3.953	−7.793	5.520	5.683	0.222
$\omega\rho5$	0.035	33.97	74	−145	−388	0.075	0.498	3.818	−7.796	5.520	5.680	0.218
$\omega\rho6$	0.04	33.73	71	−154	−387	0.076	0.509	3.690	−7.798	5.520	5.677	0.215
$\omega\rho7$	0.05	33.27	65	−168	−383	0.079	0.533	3.451	−7.803	5.520	5.671	0.209
$\omega\rho8$	0.06	32.83	60	−178	−376	0.081	0.552	3.230	−7.807	5.521	5.665	0.203

Monte Carlo (MC) techniques [34]. The band width indicates for each density the uncertainties of the calculation coming from the $3N$ interaction. At saturation density, this uncertainty is of the order of 5 MeV, ∼25%–30%.

In Fig. 2 we plot the deviation of the neutron matter pressure for each model from the microscopic results of Hebeler *et al.* [33] and Gandolfi *et al.* [34] data, in units of the pressure uncertainty ΔP of the microscopic calculations at each density, which we designate by $\sigma = \Delta P$. The light gray bands represent the microscopic calculation uncertainties, meaning that the points inside those bands are within the data limits. The dark gray bands correspond to twice the calculation uncertainties, 2σ. Except for the head of each family and Z271$\omega\rho8$, all other models agree well with the results of Ref. [33], and above $\rho = 0.05$ fm^{-3} with the MC results [34].

Models TM1, NL3, and Z271 have excessively stiff neutron matter EoS. These models do not satisfy several other constraints imposed by experiments (see Ref. [55]), in particular, the symmetry energy and/or its slope is too high, as well as the incompressibility. However, including the $\omega\rho$ or the $\sigma\rho$ terms, makes the symmetry energy softer, and we obtain some models that satisfy most of the constraints imposed in Ref. [55]. We will not consider the K_τ constraint included in Ref. [55] because it has a large uncertainty associated with it. The NL3x and Z271x models have an incompressibility at saturation, K, just above the upper limit used in Refs. [55,68], $K = 230 \pm 40$ MeV, and TM1 only satisfies this constraint within 10%. However, the incompressibility of these models is within the range $250 < K < 315$ MeV predicted in Ref. [69,70]. Therefore, we consider that the K constraint is satisfied.

Constraints at suprasaturation densities from heavy-ion collisions were also considered in Ref. [55]. For reference, in Fig. 3, we show the symmetric matter pressure as a function of the density for the models considered in this study. This plot also includes a modified Z271 model, which has an extra effective potential that will be discussed later. We compare the different EoS with the experimental results obtained from collective flow data in heavy-ion collisions [35] and from the KaoS experiment [36,71]. Only Z271 and TM1 satisfy the constraints.

Summarizing the above discussion, models TM1$\omega\rho6$, TM1$\sigma\rho6$, and Z271$\sigma\rho5$–6 satisfy the constraints imposed in Ref. [55], except the one in K_τ, the constraints from neutron matter calculations and those from Refs. [69,70]. Models NL3$\omega\rho6$ and NL3$\sigma\rho6$ only fail the flow and KaoS experiments.

B. Crust-core transition

In Fig. 4, the dynamical spinodals for the six families under study are represented. They have been obtained by solving the dispersion relation (26) for a zero-energy mode, $\omega = 0$, and taking the wave number $k = 75$ MeV. We have considered

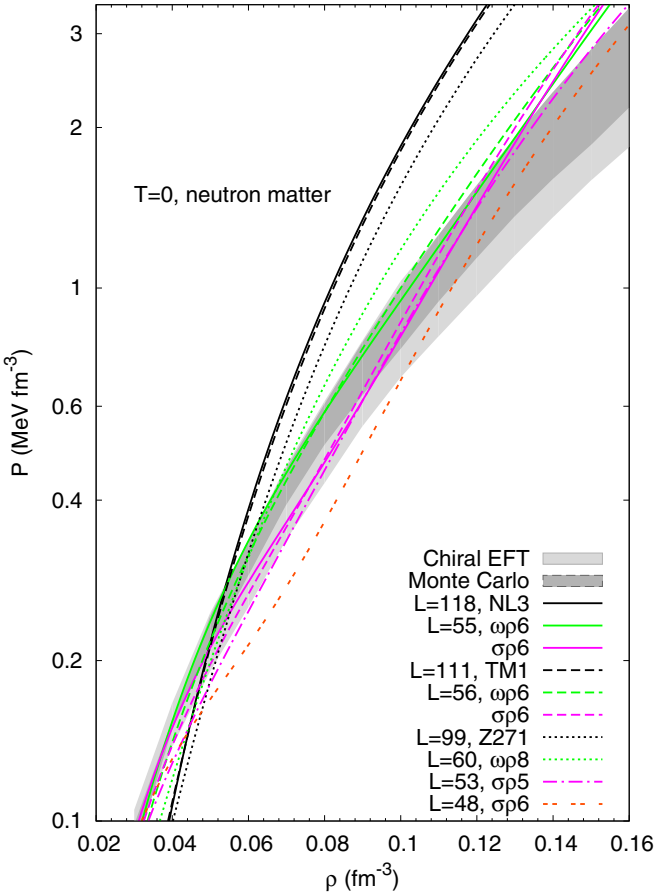

FIG. 1. Neutron matter pressure P_N as a function of the density, for some of the models considered in this study. The colored bands are the results from Ref. [33] (light gray) and [34] (dark gray).

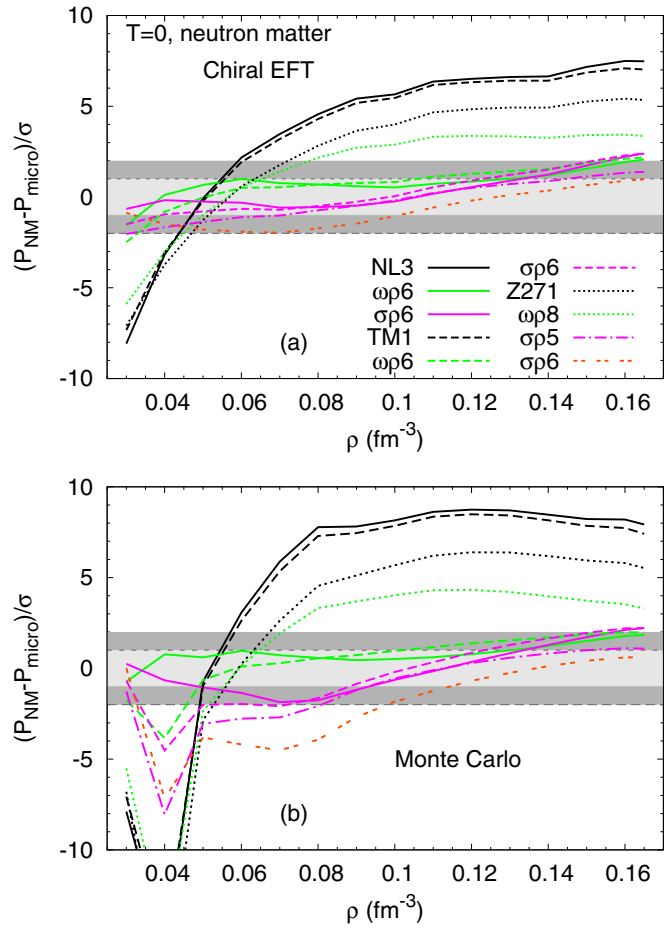

FIG. 2. Difference between the neutron matter pressure for each model and the average pressure obtained from (a) a chiral EFT [33] and (b) Monte Carlo [34] calculations, in units of the pressure uncertainty at each density, designated by $\sigma = \Delta P$. The gray bands represent the calculation uncertainty (light) and twice this uncertainty (dark). See text for more details.

this value of k because the extension of the spinodal section is close to the envelope of all spinodal sections. For NL3 and TM1, we have considered, besides the head of the family, the two parametrizations with $\omega\rho$ or $\sigma\rho$ terms that give $L = 55$ and 68 MeV; for Z271, we take the models with $L = 76$ and 60 MeV. All the values of L chosen are within the different constraints imposed in Ref. [55] for L. Some conclusions may be drawn from the figure: (i) the larger L, the smaller the spinodal section, as discussed in previous works with different models [11]; (ii) the term $\omega\rho$ makes the spinodal section larger, except for the very large isospin asymmetries, both very neutron rich or very proton rich.

The crust-core transition density ρ_t is calculated from the crossing between the spinodal sections and the EoS for β-equilibrium matter. These densities are given in Tables I and II for all models under study and are represented as a function of L in Fig. 5 (top panel). The crossing between the $\omega\rho$ and $\sigma\rho$ spinodals, for a given L, occurs close to the crossing of the β-equilibrium EoS with the spinodals and, therefore, the transition densities do not differ much, whether taking the $\omega\rho$ or the $\sigma\rho$ term. A difference, however, is seen when the transition pressures P_t are compared (see Fig. 5, bottom panel): while for the $\omega\rho$ terms, the transition pressure decreases monotonically with L, the exception being the lowest L values

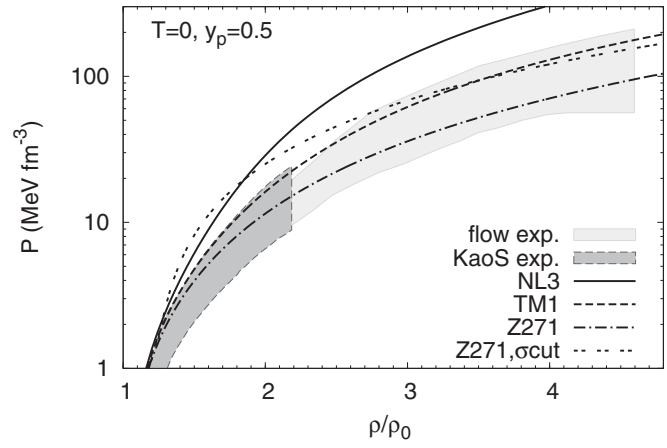

FIG. 3. Symmetric matter pressure P as a function of the density for the models considered in this study. The colored bands are the experimental results obtained from collective flow data in heavy-ion collisions [35] (light gray) and from the KaoS experiment [36,71] (dark gray).

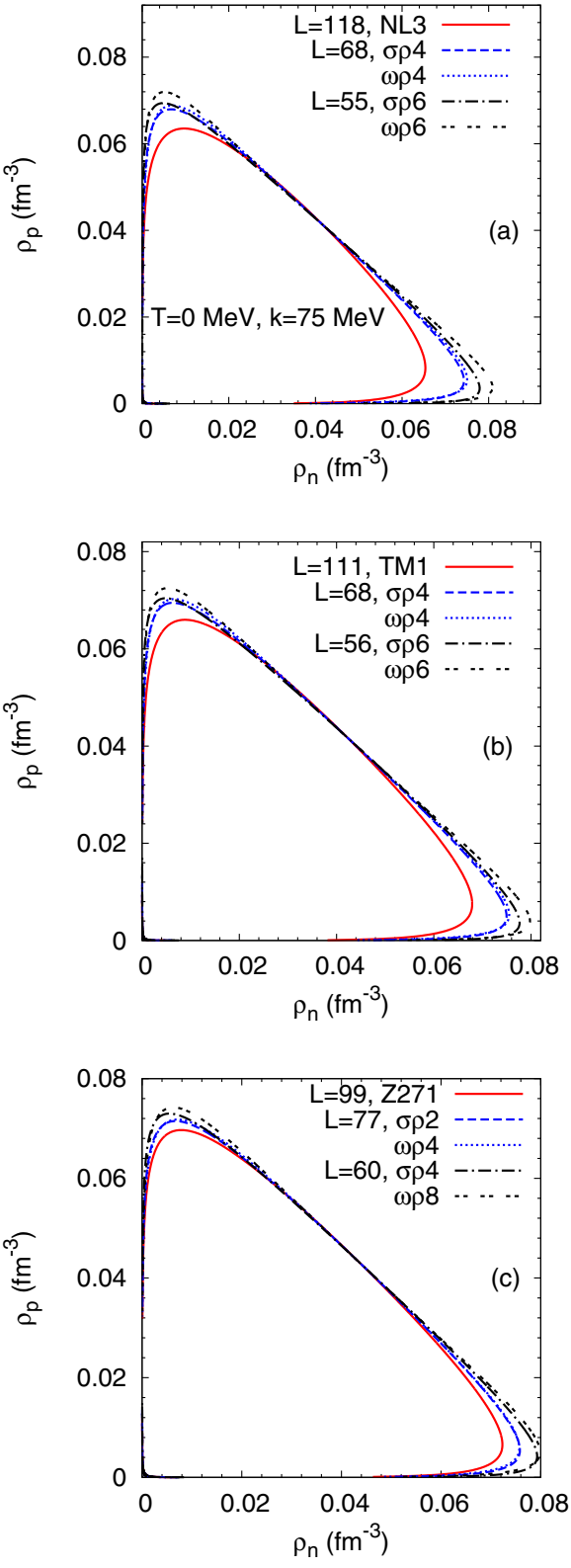

FIG. 4. Spinodal regions for the models considered.

for the TM1 and NL3 families, the $\sigma\rho$ terms gives rise to an increase of P_t with L, until $L = 70$–80 MeV, and only above this value does the pressure decrease with increasing L.

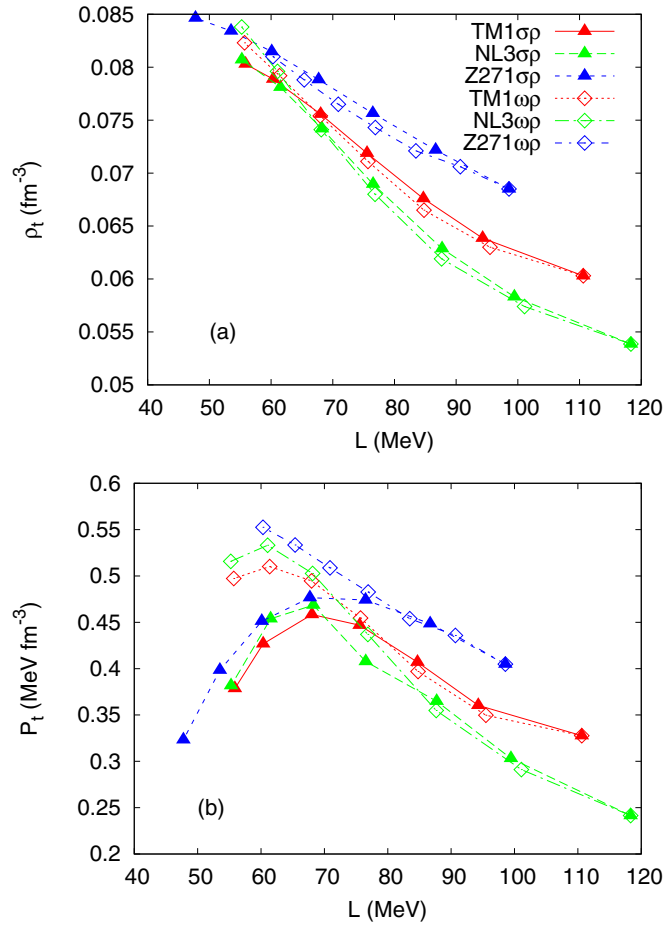

FIG. 5. Crust-core transition (a) densities ρ_t and (b) pressure P_t as a function of the slope of the symmetry energy, L.

For values of L below 80 MeV, P_t is generally larger in the models with the $\omega\rho$ term, and this difference may be as large as 25% for the smaller L shown. This difference has direct implications in the moment of inertia of the crust, which is proportional to P_t, $I_{\rm crust} \sim \frac{16\pi}{3}\frac{R_t^6 P_t}{R_s}$ in lowest order [51,54,72], where R_t is the crust thickness, and R_s is the Schwarzschild radius. Besides the transition pressure, the moment of inertia of the crust also depends on the crust thickness. In the following, we also see that the $\sigma\rho$ terms give rise to smaller crust thicknesses. This implies that smaller crust moments of inertia are expected, if the $\sigma\rho$ term is used to modify the symmetry energy.

In Fig. 6, we compare our results for the crust-core transition density with the ones obtained in Ref. [47], calculated within a relativistic random-phase approximation [73], for the Z271$\sigma\rho$ and $\omega\rho$ models, and for the NL3$\omega\rho$ family. For the Z271* models, we obtain slightly larger values for ρ_t, and this difference increases with increasing L, but even for the largest value of L, the difference is below 5%. For the NL3$\omega\rho$ models, the behavior is slightly different: for $L < 70$ MeV, our results are below those of Ref. [47], and for $L > 70$ MeV, we get larger values, although the overall difference between them is below 5%.

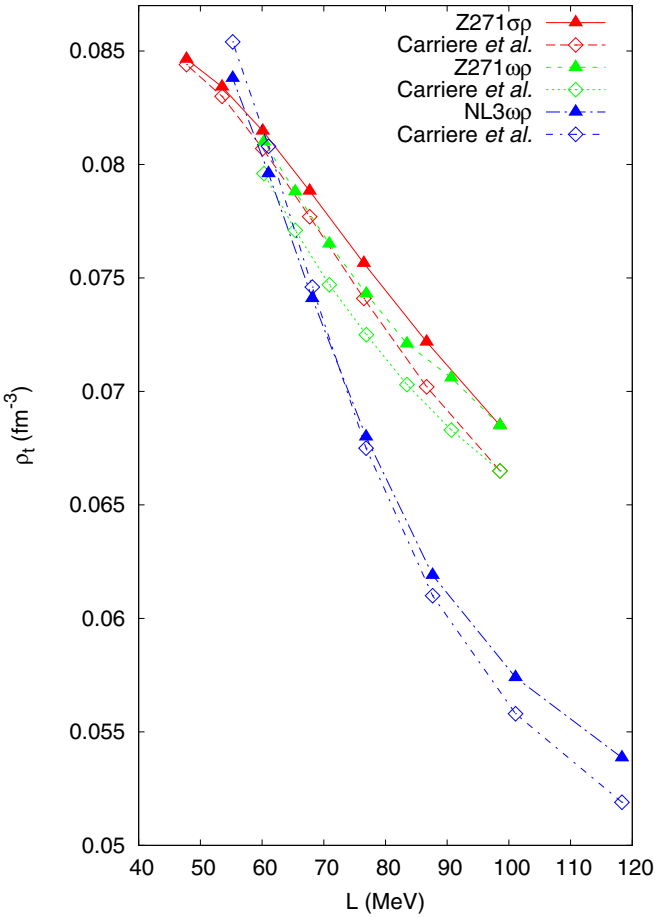

FIG. 6. Crust-core transition densities ρ_t as a function of the slope of the symmetry energy, L, where we compare with the results obtained in Ref. [47].

C. Mass-radius curves for the NL3 families

We calculate the mass-radius curves for the EoS under study by integrating the Tolmann–Oppenheimer–Volkof equations [31,32] for relativistic spherical stars in hydrostatic equilibrium. In Fig. 7, the curves for the NL3 family are shown. In order to construct the EoS of stellar matter, we take, besides the EoS of the core, the BPS EoS for the outer crust, and several models for the inner crust: (i) for models NL3$\omega\rho$ and $\sigma\rho$, we calculate the inner crust, within a Thomas–Fermi calculation [75,76]. These inner crust EoS will also be considered when building the complete stellar matter EoS, within other models with similar properties; (ii) as an alternative that tests the use of a nonunified EoS, we consider the FSU inner crust EoS [76], between the neutron drip density and the crust-core transition density, calculated within the dynamical spinodal method, for models with a similar slope L; (iii) we match directly the core EoS to the outer crust BPS EoS; (iv) the BPS plus Bethe–Baym–Pethick (BBP) EoS for densities below 0.01 fm^{-3} is matched directly to the core EoS, as suggested in Ref. [74]. Finally, we estimate the error that we introduce in quantities, such as the radius and mass, if the unified inner crust EoS is not used.

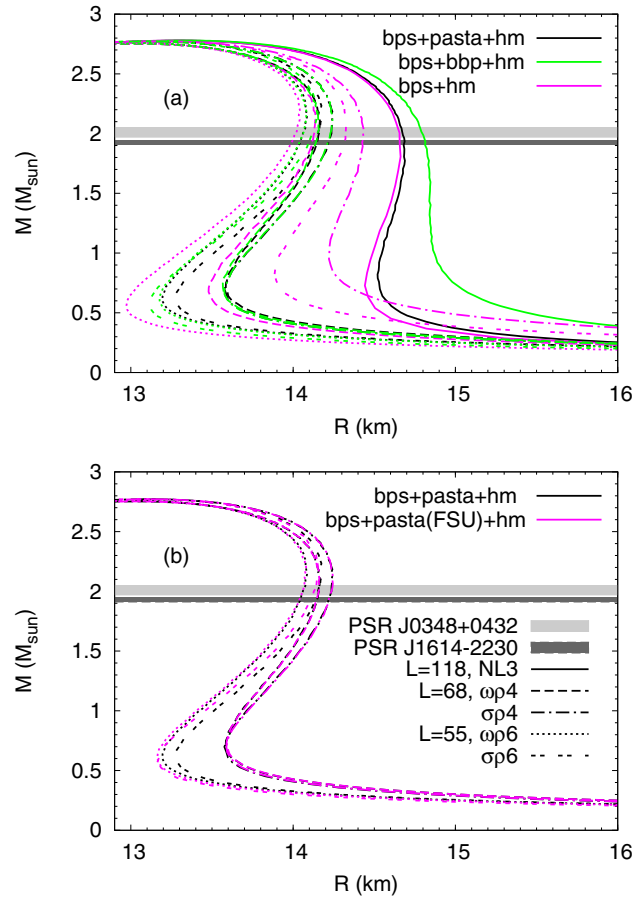

FIG. 7. $M(R)$ relations for the NL3 models: (a) BPS EoS [17] for the outer crust and the homogeneous matter EoS for the inner crust and core, bps + hm, (pink lines); the BPS + BBP [74] for the outer crust, and the homogeneous matter EoS for the inner crust and core, bps + bbp + hm, (green lines); and the BPS for the outer crust, the pasta configurations calculated from TF for the inner crust and the homogeneous matter EoS for the core, bps + pasta + hm (black lines); (b) BPS EoS for the outer crust, the pasta calculated from TF for the respective models (black lines), or for the FSU model (pink lines), for the inner crust, and the homogeneous matter EoS for the core. The horizontal bands indicate the mass uncertainties associated with the PSR J0348 + 0432 [39] and PSR J1614-2230 [40] masses.

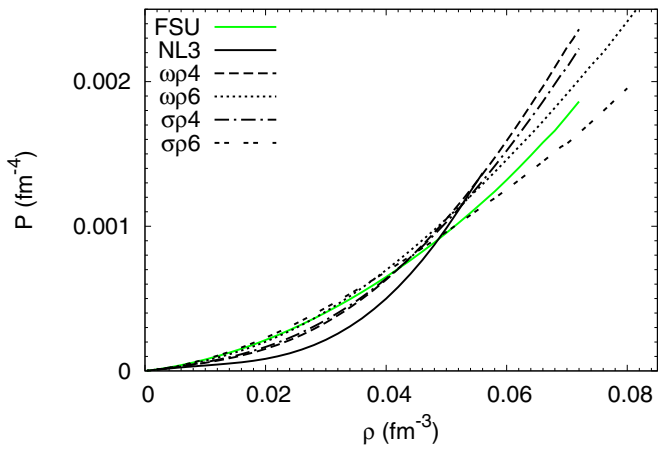

FIG. 8. Inner crust EoS considered in the present study.

TABLE III. The radius and crust thickness of a $1.4M_\odot$ star, computed with an inner crust calculated within NL3$\sigma\rho$/NL3$\omega\rho$ and FSU, or by using the BBP EoS, or without an inner crust (no ic). In all cases, we consider the BPS EoS for the outer crust.

Model	L (MeV)	$R_{1.4M_\odot}$	$\Delta R_{\rm crust}$ (NL3)	$R_{1.4M_\odot}$	$\Delta R_{\rm crust}$ (FSU)	$R_{1.4M_\odot}$	$\Delta R_{\rm crust}$ (BBP)	$R_{1.4M_\odot}$	$\Delta R_{\rm crust}$ (no ic)
NL3	118	14.630	1.325	–	–	14.847	1.508	14.594	1.249
$\omega\rho4$	68	13.928	1.450	13.928	1.377	13.916	1.453	13.879	1.416
$\omega\rho6$	55	13.753	1.425	13.745	1.432	13.749	1.432	13.671	1.355
$\sigma\rho4$	68	13.982	1.441	13.983	1.388	13.977	1.445	14.313	1.781
$\sigma\rho6$	55	13.846	1.400	13.806	1.408	13.785	1.334	14.117	1.666

In Fig. 8 and in Table VII of the Appendix, we show the inner crust EoSs that we are using in this paper. Both the FSU, the NL3, and the NL3$\omega\rho6$ inner crusts are given in Ref. [76]. In the top panel of Fig. 7, we compare the mass-radius curves for the stellar EoS obtained using the scenarios BPS plus an unified inner crust and core EoS (bps + pasta + hm) [Fig. 7(a)], the inner crust EoS is replaced by the homogeneous matter EoS (bps + hm) [Fig. 7(b)], and the BBP EoS is used for the low density inner crust EoS, and a transition to homogeneous matter occurs at $\sim$0.01 fm^{-3}, below the crust-core transition (bps + bbp + hm) [Fig. 7(c)]. Totally neglecting the inner crust EoS (dashed curves) is a quite rough approximation for all EoS, except for NL3. Although the effect on the maximum mass is negligible, the same is not true for the radius. The families of stars with an unified inner crust-core EoS (solid lines) have larger (smaller) radii than the configurations without inner crust (dashed lines) for the NL3$\omega\rho$ (NL3$\sigma\rho$) models, see Tables III and IV. Including the BBP EoS between the neutron drip and $\rho = 0.01$ fm^{-3} (dotted lines) will generally reduce the differences with respect to the unified EoS, although the improvement depends a lot on the model.

Figure 7 allows a comparison between mass-radius curves obtained with EoS whose density dependence of the symmetry energy is modified by means of a mixing $\omega\rho$ or $\sigma\rho$ term in the Lagrangian density. Within models with the same L, the $\sigma\rho$ models give slightly larger radii, the differences being larger for $M \gtrsim 1.4M_\odot$. For a $1.4M_\odot$ star, we obtained a difference of $\sim$100 m. These differences reflect themselves in the crust thickness; see Tables III and IV. The most critical approximation, giving rise to the largest error, occurs when the inner crust is completely neglected.

D. Stellar matter equations of state

Most of the times, the inner crust EoS calculated within the same model is not available. In the previous section, we tested the implications of not including the inner crust EoS, or only part of it. We now discuss the possible use of a inner crust EoS obtained for a different model. In the bottom panel of Fig. 7, we plot the mass-radius curves of stars obtained, considering for the inner crust the unified pasta calculation as before, and the inner crust EoS calculated for the FSU model, a model with the symmetry energy slope $L = 60$ MeV, not far from the slope L of NL3$\omega\rho4$, 6 and NL3$\sigma\rho4$, 6. Except for NL3$\sigma\rho6$, where we obtain a difference of $\sim$50 m ($\sim$40 m) for a $1M_\odot(1.4M_\odot)$ star, and for NL3$\omega\rho6$, where we obtain $\sim$20 m for a $1M_\odot$ star, the error on the determination of the radius is negligible for all masses. This can be better seen in Tables III and IV.

The above discussion indicates that the determination of the radii of stars requires that some care is taken when matching the crust EoS to the core EoS. Nonunified EoS may give rise to large uncertainties. It is possible, however, to build an adequate nonunified EoS, if the inner crust EoS is properly chosen. We have shown that taking the inner crust EoS of a model with similar symmetry energy properties, as the ones of the EoS used for the core, allowed the determination of the radii of the family of stars with masses above $1M_\odot$ with an uncertainty below 50 m. The inclusion of the inner crust EoS has definitely a strong effect on the radius of low- and intermediate-mass neutron stars.

For the TM1 and Z271 families, we do not have an unified EoS for the inner crust. In order to test the above conclusion, we built the stellar EoS taking for the inner crust, between the neutron drip density and the crust-core transition density, and calculated within the dynamical spinodal method, (i) the FSU EoS (thin lines) and (ii) the EoS obtained for the NL3$\omega\rho$ (dashed lines) and NL3$\sigma\rho$ (solid lines) models, choosing the EoS that has the properties closer to the ones of each one of the models of the TM1 or Z271 families (thick lines); see Fig. 9. Table V gives the correspondent maximum mass properties. In some cases, the curves (almost) coincide: this occurs for

TABLE IV. The radius and crust thickness of a $1.0M_\odot$ star, computed with an inner crust calculated within NL3$\sigma\rho$/NL3$\omega\rho$ and FSU, or by using the BBP EoS, or without an inner crust (no ic). In all cases, we consider the BPS EoS for the outer crust.

Model	L (MeV)	$R_{1M_\odot}$	$\Delta R_{\rm crust}$ (NL3)	$R_{1M_\odot}$	$\Delta R_{\rm crust}$ (FSU)	$R_{1M_\odot}$	$\Delta R_{\rm crust}$ (BBP)	$R_{1M_\odot}$	$\Delta R_{\rm crust}$ (no ic)
NL3	118	14.547	1.956	–	–	14.870	2.230	14.489	1.850
$\omega\rho4$	68	13.681	2.077	13.686	1.979	13.665	2.079	13.621	2.035
$\omega\rho6$	55	13.423	2.020	13.402	2.020	13.410	2.025	13.300	1.913
$\sigma\rho4$	68	13.713	2.057	13.720	1.99	13.710	2.067	14.223	2.581
$\sigma\rho6$	55	13.511	1.987	13.457	1.993	13.423	1.885	13.924	2.386

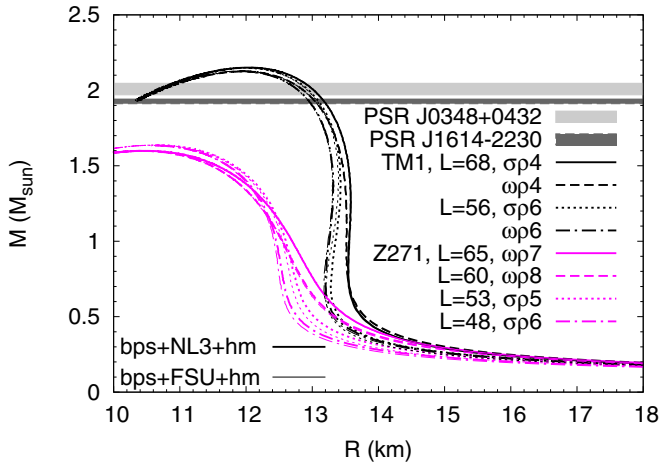

FIG. 9. $M(R)$ relations for the all the TM1 and Z271 models considered: the stellar matter EoS contains the BPS outer crust EoS, the FSU inner crust (thin lines), the NL3$\omega\rho$ or the $\sigma\rho$ (thick lines) pasta-phase EoS, and the core homogeneous matter EoS.

all models with $L > 60$ MeV. Considering the two inner crust EoS, small differences occur for models with $L < 60$ MeV, but the differences for the $1M_\odot$ ($1.4M_\odot$) are never larger than 50 (30) m. This procedure to choose the inner crust EoS seems to be a quite robust alternative to the unified inner crust EoS.

Although the symmetric nuclear matter and pure neutron matter properties of some of the Z271 models are in good agreement with experimental results or microscopic calculations, they predict an excessively small maximum-mass star. This problem can be solved by introducing an extra effective potential, dependent on the σ meson, that hinders the effective nucleon mass to stop decreasing at a density above the saturation density, as suggested in Ref. [50]. In Figure 10, we show, in the top panel, the nucleon effective mass as a function of the density for the Z271 model, with and without the σ cut potential, ΔU_f, Eq. 10 in Ref. [50], written as

$$\Delta U_f = \alpha \ln(1 + \exp[\beta(g_s\phi - f)]),$$
$$f = f_0 + c_\sigma(1 - f_0). \tag{29}$$

We have used the parameters $\beta = 1000$ and $c_\sigma = 0.05$ to be able to get maximum masses of, at least, $2M_\odot$, as shown in the bottom panel (see also Ref. [77], where they choose different parameters). f_0 and α have the same values as in Ref. [50], 0.2 and $(4.822 \times 10^{-4})m_N^4$, respectively. The stellar matter EoS were built using the BPS outer crust EoS, the most adequate NL3$\omega\rho$ or NL3$\sigma\rho$ inner crust EoS, and the homogeneous matter core EoS. The potential given in Eq. (29) does not allow constructing a EoS that simultaneously satisfies the $2M_\odot$ and the KaoS constrains; see Fig. 3.

We show in Figure 11 the mass-radius relation for the models that passed almost all constraints we considered: the ones from Ref. [55], the ones from Refs. [69,70], the microscopic neutron matter calculations [33,34], and the $2M_\odot$ observational constraint [39,40]. We note that the Z271$\sigma\rho$5–6 models fail this last constraint; however, by using the procedure of Ref. [50], we are able to get parametrizations Z271$\sigma\rho$5*–6* that describe $2M_\odot$ stars. Models NL3$\omega\rho$6, NL3$\sigma\rho$6, and Z271$\sigma\rho$5*–6* fail the flow and KaoS experiments. In Table VI, we show the properties of the $1.4M_\odot$ stars obtained with those models, together with the transition density and pressure. The following conclusions can be drawn: (i) all models predict a similar transition density and have a similar symmetry energy slope; (ii) the $\sigma\rho$ models predict a lower transition pressure, $P_t \sim 0.36 \pm 0.04$ MeV fm^{-3}, while for the $\omega\rho$ models the value is $P_t \sim 0.5$ MeV fm^{-3}; (iii) the radius and crust thickness of the $1.4M_\odot$ stars within the models that predict $2M_\odot$ stars are in the interval $13.3 \lesssim R_{1.4} \lesssim 13.9$ km and $1.3 \lesssim \Delta R \lesssim 1.4$ km, respectively.

TABLE V. Maximum mass properties. For the TM1* and Z271* models, we used for the inner crust FSU, and NL3$\omega\rho$ and $\sigma\rho$. For TM1 and Z271, we used TM1. The radii R are given in km.

Model	L (MeV)	M_g ($M_\odot$)	M_b ($M_\odot$)	R (BPS)	R (FSU)	R (NL3)	ϵ_0 (fm^{-4})	ρ_c (fm^{-3})
NL3	118	2.779	3.384	13.289	–	13.300	4.409	0.669
$\omega\rho$4	68	2.753	3.376	13.017	13.031	13.022	4.520	0.689
$\omega\rho$6	55	2.758	3.391	12.994	13.005	13.014	4.496	0.687
$\sigma\rho$4	68	2.771	3.400	13.190	13.116	13.114	4.450	0.679
$\sigma\rho$6	55	2.773	3.409	13.141	13.070	13.079	4.469	0.682
TM1	111	2.183	2.544	12.494	12.386		5.345	0.851
$\omega\rho$4	68	2.125	2.488	12.140	11.950	11.955	5.653	0.904
$\omega\rho$6	56	2.127	2.496	11.973	11.892	11.893	5.663	0.907
$\sigma\rho$4	68	2.150	2.521	12.105	12.034	12.038	5.565	0.889
$\sigma\rho$6	56	2.148	2.523	12.019	11.977	11.992	5.578	0.893
Z271	99	1.722	1.944	11.554	11.425		6.470	1.066
$\omega\rho$7	65	1.599	1.807	10.544	10.466	10.466	7.804	1.277
$\omega\rho$8	60	1.599	1.809	10.435	10.406	10.417	7.850	1.285
$\sigma\rho$5	53	1.637	1.857	10.733	10.611	10.621	7.422	1.220
$\sigma\rho$6	48	1.635	1.857	10.653	10.553	10.571	7.463	1.228

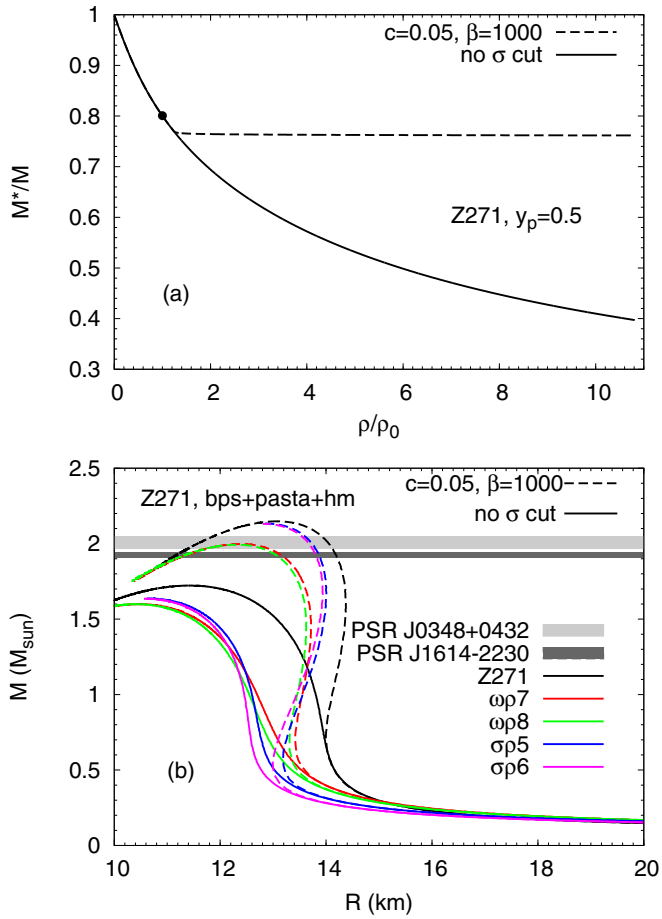

FIG. 10. (a) Nucleon effective mass as a function of density for isospin symmetric matter for the Z271 model with (dashed line) and without (solid line) the σ-cut potential. The black dot shows the effective mass at the nuclear saturation density ρ_0. (b) $M(R)$ relations for the Z271 set of models, with (dashed lines) and without (solid lines) the σ-cut potential.

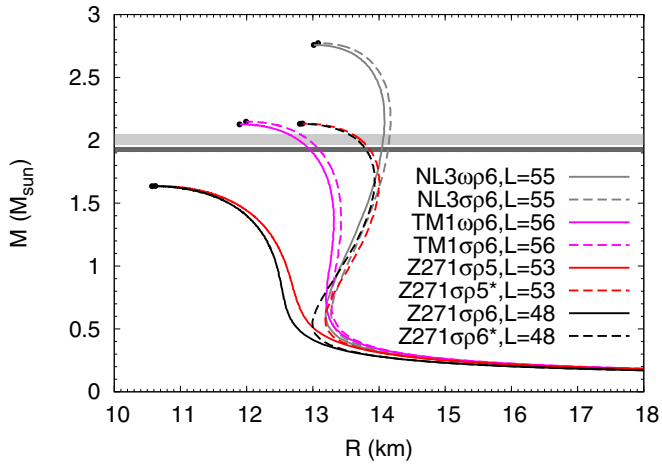

FIG. 11. Mass-radius relation of the models that passed almost all the constraints we considered. The black dots represent the maximum-mass star.

TABLE VI. Some properties of the $1.4M_\odot$ stars of the models that passed almost all the constraints, computed with an inner crust, using NL3$\sigma\rho$ or NL3$\omega\rho$. The transition pressure P_t and density ρ_t to uniform matter are also shown.

Model	L (MeV)	$R_{1.4M_\odot}$ (km)	$\Delta R_{\rm crust}$ (km)	P_t (MeV/fm^3)	ρ_t (fm^{-3})
NL3$\omega\rho$6	55	13.753	1.425	0.516	0.084
NL3$\sigma\rho$6	55	13.846	1.400	0.382	0.081
TM1$\omega\rho$6	56	13.317	1.323	0.497	0.082
TM1$\sigma\rho$6	56	13.428	1.302	0.379	0.080
Z271$\sigma\rho$5	53	12.110	1.035	0.398	0.083
Z271$\sigma\rho$5*	53	13.914	1.419	0.398	0.083
Z271$\sigma\rho$6	48	12.001	0.995	0.323	0.085
Z271$\sigma\rho$6*	48	13.833	1.389	0.323	0.085

IV. CONCLUSIONS

In the present work we have generalized the Vlasov formalism developed in previous works [8–11] with the ω-, ρ-, σ-meson terms, by including mixed terms, up to fourth order. The dispersion relation obtained allows the study of the isoscalar collective modes of nuclear matter, and the instability modes that drive the system at subsaturation densities to a nonhomogeneous phase. The dynamical spinodal surface is determined as the locus of the zero-frequency isoscalar mode. The knowledge of the dynamical spinodal and the β-equilibrium EoS is used to make a good estimation of the crust-core transition density of a neutron star.

We have applied the formalism developed to study several families of stars that differ by a mixed $\omega\rho$ or $\sigma\rho$ term which was introduced to modify the density dependence of the symmetry energy. We have analyzed the dependence of the crust-core transition density ρ_t and pressure P_t with the slope L of the model. We confirmed previous results; in particular, an almost linear anticorrelation between ρ_t and L for both mixed $\omega\rho$ or $\sigma\rho$ terms. However, in a recent publication [56], it has been shown that a nonlinear $\sigma\rho$ term of the form $\sigma\rho^2$, instead of $\sigma^2\rho^2$ as we have considered in the present work, did not show this linear behavior with L. The behavior of P_t is nonmonotonic, as discussed in Refs. [57,58], taking the $\sigma\rho$ family. However, if we consider only the $\omega\rho$ families, an anticorrelation of P_t with L is obtained. The largest transition pressures, largest crust thicknesses, and smallest radii are obtained within the $\omega\rho$ families; see also Ref. [56]. For the $\sigma\rho$ families, P_t increases (decreases) with L, for $L < 70$ ($L > 70$) MeV.

It was shown how the knowledge of the crust-core transition density enables the construction of the stellar EoS and the determination of the mass-radius curve for the family of stars, within a given model with a small radius uncertainty. For the outer crust, which extends up to the neutron drip density, the BPS EoS is considered. Between the neutron drip density and the crust-core transition density, the inner crust EoS should be taken. We have determined the inner crust EoS within a TF calculation for the $\omega\rho$ and $\sigma\rho$ NL3 family. It was shown that the error introduced in the calculation of the radius of a star with a mass above $1M_\odot$ is small if the inner crust of a model

with similar isovector saturation properties is used to describe the inner crust.

Since the Z21 family gives rise to an excessively soft EoS, a σ-dependent term was included in the Lagrangian density, as suggested in Ref. [50]. This extra term does not change the model properties at saturation density and below, but hardens the EoS above saturation density, allowing the description of $2M_\odot$, but, at the same time, not satisfying the KaoS restrictions.

We propose a set of stellar matter EoS that satisfy well-accepted saturation properties as well as constraints coming from microscopic neutron matter calculations and from experimental results. All models predict a similar transition density of the order of 0.08 fm^{-3}. However, there are differences in the transition pressure. The $\sigma\rho$ models predict a lower transition pressure than the $\omega\rho$ models. For the $1.4M_\odot$ stars, these models predict, respectively, a radius of 13.6 ± 0.3 km and a crust thickness of 1.36 ± 0.06 km. These values for $R_{1.4}$ are above the prediction of Ref. [78] but within the prediction of Ref. [16]. These crust thicknesses are $\sim$25% smaller than that obtained in Ref. [54] for the NL3max, which is close to our parametrization NL3$\omega\rho$5. We have considered the NL3max parametrization and we have obtained, by using our formalism, $P_t = 0.530$ MeV/fm^3 and $\rho_t = 0.081$ fm^{-3}, just slightly below the corresponding quantities in Ref. [54],which are 0.550 MeV/fm^3 and 0.0826 fm^{-3}, respectively. However, for the crust thickness, we have obtained $\Delta R(M = 1.4M_\odot) = 1.454$ km, that should be compared with $\Delta R(M = 1.4M_\odot) = 1.990$ km in Ref. [54]. The possible origin of this large difference is the EoS used in Ref. [54] for the inner crust EoS, a politropic that matches the BPS EoS at the neutron drip density and the homogeneous EoS at the crust-core transition. As we have shown in the present work, a nonadequate choice of the inner crust may introduce large uncertainties in the radius of low-mass stars; see also discussion in Ref. [16].

ACKNOWLEDGMENTS

H.P. is supported by Fundação para a Ciência e Tecnologia (FCT) under Project No. SFRH/BPD/95566/2013. Partial support comes from "NewCompStar", European Cooperation in Science and Technology (COST) Action MP1304. The authors acknowledge the Laboratory for Advanced Computing at the University of Coimbra for providing CPU time with the Navigator cluster. We thank S. S. Avancini for providing the finite nuclei properties code.

APPENDIX

In Table VII we present the inner crust EoS of the models NL3$\omega\rho$4, NL3$\sigma\rho$4, and NL3$\sigma\rho$6, which have been used in Sec. III C to construct the total EoS for stellar matter.

TABLE VII. Equation of state of the inner crust with pasta for the NL3$\omega\rho$4, NL3$\sigma\rho$4, and NL3$\sigma\rho$6 models. The energy density ε and pressure P are in units of fm^{-4}. The pasta inner crust EoS for FSU and NL3$\omega\rho$6 are given in Ref. [76].

ρ (fm^{-3})	NL3$\omega\rho$4		NL3$\sigma\rho$4		NL3$\sigma\rho$6	
	ε	P	ε	P	ε	P
0.002 0	0.009 529 489 093	0.952 733 262 2 $\times 10^{-5}$	0.009 524 920 955	0.907 123 740 0 $\times 10^{-5}$	0.009 525 820 613	0.983 139 671 0 $\times 10^{-5}$
0.003 0	0.014 300 051 145	0.144 937 084 8 $\times 10^{-4}$	0.014 293 017 797	0.142 403 223 4 $\times 10^{-4}$	0.014 294 951 223	0.160 140 280 1 $\times 10^{-4}$
0.004 0	0.019 072 361 290	0.198 148 245 5 $\times 10^{-4}$	0.019 062 936 306	0.198 148 245 5 $\times 10^{-4}$	0.019 066 335 633	0.232 102 047 4 $\times 10^{-4}$
0.005 0	0.023 846 043 274	0.253 386 515 4 $\times 10^{-4}$	0.023 834 312 335	0.257 947 485 8 $\times 10^{-4}$	0.023 839 607 835	0.310 651 885 2 $\times 10^{-4}$
0.006 0	0.028 620 865 196	0.311 158 655 7 $\times 10^{-4}$	0.028 606 912 121	0.319 773 789 7 $\times 10^{-4}$	0.028 614 535 928	0.396 296 491 1 $\times 10^{-4}$
0.007 0	0.033 396 668 732	0.370 957 859 6 $\times 10^{-4}$	0.033 380 579 203	0.385 654 275 3 $\times 10^{-4}$	0.033 390 954 137	0.488 529 185 5 $\times 10^{-4}$
0.008 0	0.038 173 336 536	0.432 277 411 2 $\times 10^{-4}$	0.038 155 212 998	0.454 068 649 6 $\times 10^{-4}$	0.038 168 746 978	0.587 856 702 6 $\times 10^{-4}$
0.009 0	0.042 950 786 650	0.497 144 319 5 $\times 10^{-4}$	0.042 930 707 335	0.525 523 646 5 $\times 10^{-4}$	0.042 947 817 594	0.693 772 308 3 $\times 10^{-4}$
0.010 0	0.047 728 978 097	0.564 038 418 8 $\times 10^{-4}$	0.047 707 032 412	0.601 539 577 5 $\times 10^{-4}$	0.047 728 102 654	0.806 275 857 0 $\times 10^{-4}$
0.011 0	0.052 507 854 998	0.634 986 572 5 $\times 10^{-4}$	0.052 484 132 349	0.681 102 974 3 $\times 10^{-4}$	0.052 509 546 280	0.925 367 567 1 $\times 10^{-4}$
0.012 0	0.057 287 395 000	0.710 495 805 8 $\times 10^{-4}$	0.057 261 981 070	0.765 227 305 2 $\times 10^{-4}$	0.057 292 107 493	0.105 054 052 3 $\times 10^{-3}$
0.013 0	0.062 067 583 203	0.789 552 432 3 $\times 10^{-4}$	0.062 040 548 772	0.854 926 111 1 $\times 10^{-4}$	0.062 075 737 864	0.118 331 503 5 $\times 10^{-3}$
0.014 0	0.066 848 404 706	0.874 690 231 3 $\times 10^{-4}$	0.066 819 831 729	0.950 199 464 6 $\times 10^{-4}$	0.066 860 415 041	0.132 217 086 5 $\times 10^{-3}$
0.015 0	0.071 629 844 606	0.964 895 807 6 $\times 10^{-4}$	0.071 599 796 414	0.105 054 052 3 $\times 10^{-3}$	0.071 646 101 773	0.146 761 478 4 $\times 10^{-3}$
0.016 0	0.076 411 917 806	0.106 219 624 3 $\times 10^{-3}$	0.076 380 468 905	0.115 797 636 7 $\times 10^{-3}$	0.076 432 794 333	0.161 964 664 6 $\times 10^{-3}$
0.017 0	0.081 194 624 305	0.116 659 146 4 $\times 10^{-3}$	0.081 161 834 300	0.127 250 707 0 $\times 10^{-3}$	0.081 220 448 017	0.177 877 344 0 $\times 10^{-3}$
0.018 0	0.085 977 941 751	0.127 757 477 5 $\times 10^{-3}$	0.085 943 877 697	0.139 261 232 1 $\times 10^{-3}$	0.086 009 055 376	0.194 347 463 5 $\times 10^{-3}$
0.019 0	0.090 761 914 849	0.139 717 318 2 $\times 10^{-3}$	0.090 726 628 900	0.152 183 944 0 $\times 10^{-3}$	0.090 798 601 508	0.211 476 392 0 $\times 10^{-3}$
0.020 0	0.095 546 536 148	0.152 488 006 3 $\times 10^{-3}$	0.095 510 080 457	0.165 917 488 6 $\times 10^{-3}$	0.095 589 056 611	0.229 264 114 8 $\times 10^{-3}$
0.021 0	0.100 331 813 097	0.166 069 527 0 $\times 10^{-3}$	0.100 294 232 368	0.180 360 526 4 $\times 10^{-3}$	0.100 380 428 135	0.247 609 306 8 $\times 10^{-3}$
0.022 0	0.105 117 775 500	0.180 664 588 7 $\times 10^{-3}$	0.105 079 092 085	0.195 715 736 5 $\times 10^{-3}$	0.105 172 678 828	0.266 562 623 4 $\times 10^{-3}$
0.023 0	0.109 904 408 455	0.196 222 521 5 $\times 10^{-3}$	0.109 864 674 509	0.211 983 162 4 $\times 10^{-3}$	0.109 965 816 140	0.286 073 365 7 $\times 10^{-3}$
0.024 0	0.114 691 741 765	0.212 641 971 3 $\times 10^{-3}$	0.114 650 979 638	0.229 010 722 3 $\times 10^{-3}$	0.114 759 802 818	0.306 141 591 9 $\times 10^{-3}$
0.025 0	0.119 479 775 429	0.230 226 985 9 $\times 10^{-3}$	0.119 438 014 925	0.247 153 191 6 $\times 10^{-3}$	0.119 554 653 764	0.326 767 243 7 $\times 10^{-3}$

TABLE VII. *(Continued.)*

ρ (fm^{-3})	NL3$\omega\rho$4		NL3$\sigma\rho$4		NL3$\sigma\rho$6	
	ε	P	ε	P	ε	P
0.026 0	0.124 268 546 700	$0.248\,724\,187\,3 \times 10^{-3}$	0.124 225 787 818	$0.266\,157\,207\,1 \times 10^{-3}$	0.124 350 324 273	$0.347\,849\,010\,7 \times 10^{-3}$
0.027 0	0.129 058 048 129	$0.268\,437\,666\,8 \times 10^{-3}$	0.129 014 313 221	$0.286\,022\,695\,9 \times 10^{-3}$	0.129 146 814 346	$0.369\,488\,232\,5 \times 10^{-3}$
0.028 0	0.133 848 294 616	$0.289\,266\,055\,9 \times 10^{-3}$	0.133 803 606 033	$0.307\,003\,094\,3 \times 10^{-3}$	0.133 944 109 082	$0.391\,532\,870\,7 \times 10^{-3}$
0.029 0	0.138 639 286 160	$0.311\,006\,617\,3 \times 10^{-3}$	0.138 593 643 904	$0.328\,946\,393\,0 \times 10^{-3}$	0.138 742 208 481	$0.414\,084\,264\,8 \times 10^{-3}$
0.030 0	0.143 431 067 467	$0.334\,115\,466\,1 \times 10^{-3}$	0.143 384 456 635	$0.351\,751\,194\,1 \times 10^{-3}$	0.143 541 097 641	$0.437\,193\,084\,5 \times 10^{-3}$
0.031 0	0.148 223 638 535	$0.358\,389\,894\,2 \times 10^{-3}$	0.148 176 059 127	$0.375\,772\,215\,2 \times 10^{-3}$	0.148 340 746 760	$0.460\,504\,670\,6 \times 10^{-3}$
0.032 0	0.153 017 029 166	$0.383\,880\,571\,5 \times 10^{-3}$	0.152 968 466 282	$0.400\,806\,777\,2 \times 10^{-3}$	0.153 141 170 740	$0.484\,069\,576\,5 \times 10^{-3}$
0.033 0	0.157 811 194 658	$0.410\,283\,450\,0 \times 10^{-3}$	0.157 761 648 297	$0.426\,601\,531\,2 \times 10^{-3}$	0.157 942 339 778	$0.508\,394\,674\,4 \times 10^{-3}$
0.034 0	0.162 606 209 517	$0.438\,155\,984\,7 \times 10^{-3}$	0.162 555 649 877	$0.453\,713\,903\,0 \times 10^{-3}$	0.162 744 253 874	$0.532\,821\,170\,1 \times 10^{-3}$
0.035 0	0.167 402 043 939	$0.467\,244\,739\,4 \times 10^{-3}$	0.167 350 441 217	$0.481\,839\,815\,6 \times 10^{-3}$	0.167 546 868 324	$0.557\,653\,023\,9 \times 10^{-3}$
0.036 0	0.172 198 727 727	$0.497\,296\,394\,3 \times 10^{-3}$	0.172 146 052 122	$0.511\,080\,608\,7 \times 10^{-3}$	0.172 350 198 030	$0.582\,789\,012\,7 \times 10^{-3}$
0.037 0	0.176 996 275 783	$0.528\,817\,647\,1 \times 10^{-3}$	0.176 942 497 492	$0.541\,030\,895\,0 \times 10^{-3}$	0.177 154 257 894	$0.608\,178\,321\,3 \times 10^{-3}$
0.038 0	0.181 794 673 204	$0.561\,605\,906\,1 \times 10^{-3}$	0.181 739 777 327	$0.572\,349\,468\,7 \times 10^{-3}$	0.181 958 958 507	$0.633\,922\,405\,5 \times 10^{-3}$
0.039 0	0.186 593 979 597	$0.595\,610\,356\,0 \times 10^{-3}$	0.186 537 876 725	$0.604\,681\,554\,3 \times 10^{-3}$	0.186 764 389 277	$0.659\,869\,168\,9 \times 10^{-3}$
0.040 0	0.191 394 165 158	$0.630\,577\,676\,9 \times 10^{-3}$	0.191 336 825 490	$0.638\,128\,607\,5 \times 10^{-3}$	0.191 570 460 796	$0.686\,170\,649\,7 \times 10^{-3}$
0.041 0	0.196 195 229 888	$0.667\,116\,022\,7 \times 10^{-3}$	0.196 136 608 720	$0.672\,285\,095\,8 \times 10^{-3}$	0.196 377 217 770	$0.712\,674\,926\,0 \times 10^{-3}$
0.042 0	0.200 997 203 588	$0.704\,870\,617\,5 \times 10^{-3}$	0.200 937 271 118	$0.707\,809\,871\,5 \times 10^{-3}$	0.201 184 600 592	$0.739\,381\,823\,2 \times 10^{-3}$
0.043 0	0.205 800 086 260	$0.743\,537\,442\,8 \times 10^{-3}$	0.205 738 782 883	$0.744\,348\,217\,3 \times 10^{-3}$	0.205 992 653 966	$0.766\,342\,156\,6 \times 10^{-3}$
0.044 0	0.210 603 877 902	$0.783\,825\,875\,3 \times 10^{-3}$	0.210 541 129 112	$0.781\,950\,831\,9 \times 10^{-3}$	0.210 801 303 387	$0.793\,505\,227\,2 \times 10^{-3}$
0.045 0	0.215 408 638 120	$0.825\,279\,916\,2 \times 10^{-3}$	0.215 344 354 510	$0.820\,364\,162\,8 \times 10^{-3}$	0.215 610 593 557	$0.820\,921\,617\,6 \times 10^{-3}$
0.046 0	0.220 214 262 605	$0.868\,000\,846\,8 \times 10^{-3}$	0.220 148 459 077	$0.860\,044\,499\,9 \times 10^{-3}$	0.220 420 479 774	$0.848\,743\,482\,5 \times 10^{-3}$
0.047 0	0.225 020 855 665	$0.911\,634\,066\,1 \times 10^{-3}$	0.224 953 413 010	$0.900\,789\,105\,8 \times 10^{-3}$	0.225 230 976 939	$0.876\,565\,289\,2 \times 10^{-3}$
0.048 0	0.229 828 447 104	$0.956\,838\,193\,8 \times 10^{-3}$	0.229 759 275 913	$0.942\,547\,165\,3 \times 10^{-3}$	0.230 042 085 052	$0.904\,589\,833\,2 \times 10^{-3}$
0.049 0	0.234 636 932 611	$0.100\,325\,862\,9 \times 10^{-2}$	0.234 565 988 183	$0.985\,065\,475\,1 \times 10^{-3}$	0.234 853 759 408	$0.932\,867\,813\,4 \times 10^{-3}$
0.050 0	0.239 446 416 497	$0.105\,084\,455\,6 \times 10^{-2}$	0.239 373 609 424	$0.102\,890\,131\,5 \times 10^{-2}$	0.239 666 014 910	$0.961\,297\,715\,5 \times 10^{-3}$
0.051 0	0.244 256 809 354	$0.109\,934\,271\,3 \times 10^{-2}$	0.244 182 094 932	$0.107\,380\,130\,8 \times 10^{-2}$	0.244 478 836 656	$0.989\,981\,112\,1 \times 10^{-3}$
0.052 0	0.249 068 230 391	$0.114\,925\,985\,7 \times 10^{-2}$	0.248 991 489 410	$0.111\,966\,428\,8 \times 10^{-2}$	0.249 292 254 448	$0.101\,896\,852\,7 \times 10^{-2}$
0.053 0	0.253 880 590 200	$0.120\,049\,470\,6 \times 10^{-2}$	0.253 801 763 058	$0.116\,649\,013\,9 \times 10^{-2}$	0.254 106 193 781	$0.104\,805\,734\,0 \times 10^{-2}$
0.054 0	0.258 693 933 487	$0.125\,289\,498\,8 \times 10^{-2}$	0.258 612 930 775	$0.121\,407\,618\,3 \times 10^{-2}$	0.258 920 729 160	$0.107\,729\,807\,5 \times 10^{-2}$
0.055 0	0.263 508 260 250	$0.130\,641\,018\,0 \times 10^{-2}$	0.263 424 992 561	$0.126\,313\,173\,7 \times 10^{-2}$	0.263 735 800 982	$0.110\,689\,364\,4 \times 10^{-2}$
0.056 0	0.268 323 540 688	$0.136\,109\,092\,3 \times 10^{-2}$	0.268 237 978 220	$0.131\,299\,824\,0 \times 10^{-2}$	0.268 551 379 442	$0.113\,674\,253\,2 \times 10^{-2}$
0.057 0	0.273 139 834 404	$0.141\,658\,261\,4 \times 10^{-2}$	0.273 051 828 146	$0.136\,387\,825\,5 \times 10^{-2}$	0.273 367 494 345	$0.116\,674\,357\,6 \times 10^{-2}$
0.058 0	0.277 957 081 795	$0.147\,359\,469\,0 \times 10^{-2}$	0.277 866 572 142	$0.141\,577\,189\,8 \times 10^{-2}$	0.278 184 115 887	$0.119\,345\,041\,5 \times 10^{-2}$
0.059 0	0.282 775 372 267	$0.153\,182\,284\,0 \times 10^{-2}$	0.282 682 240 009	$0.146\,862\,817\,9 \times 10^{-2}$	0.283 001 244 068	$0.122\,421\,165\,0 \times 10^{-2}$
0.060 0	0.287 594 646 215	$0.159\,081\,129\,8 \times 10^{-2}$	0.287 498 801 947	$0.152\,239\,692\,4 \times 10^{-2}$	0.287 818 878 889	$0.125\,512\,469\,1 \times 10^{-2}$
0.061 0	0.292 414 903 641	$0.165\,116\,787\,0 \times 10^{-2}$	0.292 316 287 756	$0.157\,728\,034\,5 \times 10^{-2}$	0.292 637 050 152	$0.128\,634\,192\,5 \times 10^{-2}$
0.062 0	0.297 236 144 543	$0.171\,263\,946\,7 \times 10^{-2}$	0.297 134 667 635	$0.163\,287\,343\,5 \times 10^{-2}$	0.297 455 728 054	$0.131\,791\,399\,3 \times 10^{-2}$
0.063 0	0.302 058 428 526	$0.177\,507\,393\,5 \times 10^{-2}$	0.301 954 001 188	$0.168\,958\,131\,7 \times 10^{-2}$	0.302 274 912 596	$0.134\,973\,926\,5 \times 10^{-2}$
0.064 0	0.306 881 725 788	$0.183\,872\,471\,1 \times 10^{-2}$	0.306 774 199 009	$0.174\,720\,143\,0 \times 10^{-2}$	0.307 094 633 579	$0.138\,191\,937\,0 \times 10^{-2}$
0.065 0	0.311 706 036 329	$0.190\,293\,265\,0 \times 10^{-2}$	0.311 595 320 702	$0.180\,254\,096\,6 \times 10^{-2}$	0.311 914 891 005	$0.141\,470\,751\,3 \times 10^{-2}$
0.066 0	0.316 531 240 940	$0.196\,516\,444\,0 \times 10^{-2}$	0.316 417 217 255	$0.186\,223\,886\,0 \times 10^{-2}$	0.316 735 535 860	$0.144\,759\,728\,6 \times 10^{-2}$
0.067 0	0.321 357 458 830	$0.203\,150\,091\,7 \times 10^{-2}$	0.321 240 127 087	$0.192\,259\,543\,1 \times 10^{-2}$	0.321 556 776 762	$0.148\,099\,346\,6 \times 10^{-2}$
0.068 0	0.326 184 719 801	$0.209\,930\,725\,4 \times 10^{-2}$	0.326 063 960 791	$0.198\,391\,499\,0 \times 10^{-2}$	0.326 378 494 501	$0.151\,449\,115\,9 \times 10^{-2}$
0.069 0	0.331 013 083 458	$0.216\,716\,411\,5 \times 10^{-2}$	0.330 888 777 971	$0.204\,574\,130\,5 \times 10^{-2}$	0.331 200 808 287	$0.154\,885\,044\,3 \times 10^{-2}$
0.070 0	0.335 842 400 789	$0.223\,613\,600\,2 \times 10^{-2}$	0.335 714 370 012	$0.209\,824\,298\,5 \times 10^{-2}$	0.336 023 390 293	$0.157\,109\,776\,0 \times 10^{-2}$
0.071 0	0.340 671 092 272	$0.229\,471\,898\,6 \times 10^{-2}$	0.340 540 796 518	$0.216\,331\,263\,1 \times 10^{-2}$	0.340 846 419 334	$0.160\,626\,787\,7 \times 10^{-2}$
0.072 0	0.345 502 316 952	$0.236\,176\,489\,9 \times 10^{-2}$	0.345 368 176 699	$0.222\,848\,379\,1 \times 10^{-2}$	0.345 669 955 015	$0.164\,387\,037\,5 \times 10^{-2}$
0.073 0					0.350 494 056 940	$0.168\,091\,559\,3 \times 10^{-2}$
0.074 0					0.355 318 605 900	$0.171\,851\,797\,5 \times 10^{-2}$
0.075 0					0.360 143 750 906	$0.175\,662\,734\,5 \times 10^{-2}$
0.076 0					0.364 969 402 552	$0.179\,575\,022\,8 \times 10^{-2}$
0.077 0					0.369 795 531 034	$0.183\,482\,246\,9 \times 10^{-2}$
0.078 0					0.374 622 225 761	$0.187\,460\,414\,6 \times 10^{-2}$
0.079 0					0.379 449 486 732	$0.191\,433\,518\,2 \times 10^{-2}$
0.080 0					0.384 277 373 552	$0.195\,366\,074\,3 \times 10^{-2}$

[1] H. H. K. Tang, C. H. Dasso, H. Esbensen, R. A. Broglia, and A. Winther, Phys. Lett. B **101**, 10 (1981).
[2] X. Jin, Y. X. Zhang, and M. Sano, Nucl. Phys. A **506**, 655 (1989).
[3] C. M. Ko and Q. Li, Phys. Rev. C **37**, 2270 (1988).
[4] C. M. Ko, Q. Li, and R. Wang, Phys. Rev. Lett. **59**, 1084 (1987).
[5] Q. Li and C. M. Ko, Mod. Phys. Lett. A **3**, 465 (1988).
[6] M. Nielsen, C. Providência, and J. da Providência, Phys. Rev. C **44**, 209 (1991).
[7] M. Nielsen, C. Providência, and J. da Providência, Phys. Rev. C **47**, 200 (1993).
[8] S. S. Avancini, L. Brito, D. P. Menezes, and C. Providência, Phys. Rev. C **71**, 044323 (2005).
[9] C. Providência, L. Brito, A. M. S. Santos, D. P. Menezes, and S. S. Avancini, Phys. Rev. C **74**, 045802 (2006).
[10] H. Pais, A. Santos, and C. Providência, Phys. Rev. C **80**, 045808 (2009).
[11] H. Pais, A. Santos, L. Brito, and C. Providência, Phys. Rev. C **82**, 025801 (2010).
[12] A. M. Santos, L. Brito, and C. Providência, Phys. Rev. C **77**, 045805 (2008).
[13] S. S. Avancini, S. Chiacchiera, D. P. Menezes, and C. Providência, Phys. Rev. C **82**, 055807 (2010).
[14] S. S. Avancini, S. Chiacchiera, D. P. Menezes, and C. Providência, Phys. Rev. C **85**, 059904(E) (2012).
[15] C. J. Pethick, D. J. Ravenhall, and C. P. Lorenz, Nucl. Phys. A **584**, 675 (1995).
[16] M. Fortin, C. Providência, A. R. Raduta, F. Gulminelli, J. L. Zdunik, P. Haensel, and M. Bejger, arXiv:1604.01944.
[17] G. Baym, C. Pethick, and P. Sutherland, Astrophys. J. **170**, 299 (1971).
[18] P. Haensel and B. Pichon, Astron. Astrophys. **283**, 313 (1994).
[19] S. B. Rüster, M. Hempel, and J. Schaffner-Bielich, Phys. Rev. C **73**, 035804 (2006).
[20] D. G. Ravenhall, C. J. Pethick, and J. R. Wilson, Phys. Rev. Lett. **50**, 2066 (1983).
[21] G. Watanabe, H. Sonoda, T. Maruyama, K. Sato, K. Yasuoka, and T. Ebisuzaki, Phys. Rev. Lett. **103**, 121101 (2009).
[22] C. J. Horowitz, M. A. Pérez-García, D. K. Berry, and J. Piekarewicz, Phys. Rev. C **72**, 035801 (2005).
[23] A. S. Schneider, D. K. Berry, M. E. Caplan, C. J. Horowitz, and Z. Lin, Phys. Rev. C **93**, 065806 (2016).
[24] C. O. Dorso, P. A. Giménez Molinelli, and J. A. López, Phys. Rev. C **86**, 055805 (2012).
[25] W. G. Newton and J. R. Stone, Phys. Rev. C **79**, 055801 (2009).
[26] H. Pais and J. R. Stone, Phys. Rev. Lett. **109**, 151101 (2012).
[27] T. Maruyama, T. Tatsumi, D. N. Voskresensky, T. Tanigawa, and S. Chiba, Phys. Rev. C **72**, 015802 (2005).
[28] S. S. Avancini and B. P. Bertolino, Int. J. Mod. Phys. E **24**, 1550078 (2015).
[29] M. Okamoto, T. Maruyama, K. Yabana, and T. Tatsumi, Phys. Rev. C **88**, 025801 (2013).
[30] J. A. Pons, D. Viganò, and N. Rea, Nat. Phys. **9**, 431 (2013).
[31] R. C. Tolman, Phys. Rev. **55**, 364 (1939).
[32] J. R. Oppenheimer and G. M. Volkoff, Phys. Rev. **55**, 374 (1939).
[33] K. Hebeler, J. M. Lattimer, C. J. Pethick, and A. Schwenk, Astrophys. J. **773**, 11 (2013).
[34] S. Gandolfi, J. Carlson, and S. Reddy, Phys. Rev. C **85**, 032801 (2012).
[35] P. Danielewicz, R. Lacey, and W. G. Lynch, Science **298**, 1592 (2002).
[36] W. G. Lynch, M. B. Tsang, Y. Zhang, P. Danielewicz, M. Famiano, Z. Li, and A. W. Steiner, Prog. Part. Nucl. Phys. **62**, 427 (2009).
[37] M. B. Tsang, J. R. Stone, F. Camera, P. Danielewicz, S. Gandolfi, K. Hebeler, C. J. Horowitz, J. Lee, W. G. Lynch, Z. Kohley, R. Lemmon, P. Möller, T. Murakami, S. Riordan, X. Roca-Maza, F. Sammarruca, A. W. Steiner, I. Vidaña, and S. J. Yennello, Phys. Rev. C **86**, 015803 (2012).
[38] P. B. Demorest, T. Pennucci, S. M. Ransom, M. S. E. Roberts, and J. W. T. Hessels, Nature (London) **467**, 1081 (2010).
[39] J. Antoniadis, P. C. C. Freire, N. Wex, T. M. Tauris, R. S. Lynch, M. H. van Kerkwijk, M. Kramer, C. Bassa, V. S. Dhillon, T. Driebe, J. W. T. Hessels, V. M. Kaspi, V. I. Kondratiev, N. Langer, T. R. Marsh, M. A. McLaughlin, T. T. Pennucci, S. M. Ransom, I. H. Stairs, J. van Leeuwen, J. P. W. Verbiest, and D. G. Whelan, Science **340**, 448 (2013).
[40] E. Fonseca, T. T. Pennucci, J. A. Ellis, I. H. Stairs, D. J. Nice, S. M. Ransom, P. B. Demorest, Z. Arzoumanian, K. Crowter, T. Dolch, R. D. Ferdman, M. E. Gonzalez, G. Jones, M. L. Jones, M. T. Lam, L. Levin, M. A. McLaughlin, K. Stovall, J. K. Swiggum, and W. Zhu, arXiv:1603.00545.
[41] D. Barret, K. Nandra, X. Barcons, A. Fabian, J. W. den Herder, L. Piro, M. Watson, J. Aird, G. Branduardi-Raymont, M. Cappi, F. Carrera, A. Comastri, E. Costantini, J. Croston, A. Decourchelle, C. Done, M. Dovciak, S. Ettori, A. Finoguenov, A. Georgakakis, P. Jonker, J. Kaastra, G. Matt, C. Motch, P. O'Brien, G. Pareschi, E. Pointecouteau, G. Pratt, G. Rauw, T. Reiprich, J. Sanders, S. Sciortino, R. Willingale, and J. Wilms, in *SF2A-2013 Proceedings*, edited by L. Cambresy, F. Martins, E. Nuss, and A. Palacios (Societé Française d'Astronomie et d'Astrophysique (SF2A), Montpellier, 2013), pp. 447–453.
[42] G. A. Lalazissis, J. König, and P. Ring, Phys. Rev. C **55**, 540 (1997).
[43] J. M. Lattimer, Annu. Rev. Nucl. Part. Sci. **62**, 485 (2012).
[44] S. Weissenborn, D. Chatterjee, and J. Schaffner-Bielich, Nucl. Phys. A **881**, 62 (2012).
[45] L. Bonanno and A. Sedrakian, Astron. Astrophys. **539**, A16 (2012).
[46] C. J. Horowitz and J. Piekarewicz, Phys. Rev. Lett. **86**, 5647 (2001).
[47] J. Carriere, C. J. Horowitz, and J. Piekarewicz, Astrophys. J. **593**, 463 (2003).
[48] Y. Sugahara and H. Toki, Nucl. Phys. A **579**, 557 (1994).
[49] G. Shen, C. J. Horowitz, and E. O'Connor, Phys. Rev. C **83**, 065808 (2011).
[50] K. A. Maslov, E. E. Kolomeitsev, and D. N. Voskresensky, Phys. Rev. C **92**, 052801 (2015).
[51] B. Link, R. I. Epstein, and J. M. Lattimer, Phys. Rev. Lett. **83**, 3362 (1999).
[52] N. Chamel, Phys. Rev. Lett. **110**, 011101 (2013).
[53] N. Andersson, K. Glampedakis, W. C. G. Ho, and C. M. Espinoza, Phys. Rev. Lett. **109**, 241103 (2012).
[54] J. Piekarewicz, F. J. Fattoyev, and C. J. Horowitz, Phys. Rev. C **90**, 015803 (2014).
[55] M. Dutra, O. Lourenço, S. S. Avancini, B. V. Carlson, A. Delfino, D. P. Menezes, C. Providência, S. Typel, and J. R. Stone, Phys. Rev. C **90**, 055203 (2014).
[56] H. Pais, A. Sulaksono, B. K. Agrawal, and C. Providência, Phys. Rev. C **93**, 045802 (2016).

[57] C. Ducoin, J. Margueron, and C. Providência, Europhys. Lett. **91**, 32001 (2010).
[58] C. Ducoin, J. Margueron, C. Providência, and I. Vidaña, Phys. Rev. C **83**, 045810 (2011).
[59] R. J. Furnstahl, B. D. Serot, and H. B. Tang, Nucl. Phys. A **598**, 539 (1996).
[60] R. J. Furnstahl, B. D. Serot, and H. B. Tang, Nucl. Phys. A **615**, 441 (1997).
[61] A. Sulaksono and Kasmudin, Phys. Rev. C **80**, 054317 (2009).
[62] B. K. Agrawal, Phys. Rev. C **81**, 034323 (2010).
[63] J. D. Walecka, Ann. Phys. (NY) **83**, 491 (1974).
[64] S. S. Avancini, L. Brito, D. P. Menezes, and C. Providência, Phys. Rev. C **70**, 015203 (2004).
[65] C. Providência, L. Brito, S. S. Avancini, D. P. Menezes, and P. Chomaz, Phys. Rev. C **73**, 025805 (2006).
[66] K. Sumiyoshi, H. Kuwabara, and H. Toki, Nucl. Phys. A **581**, 725 (1995).
[67] I. Vidaña, C. Providência, A. Polls, and A. Rios, Phys. Rev. C **80**, 045806 (2009).
[68] E. Khan, J. Margueron, and I. Vidaña, Phys. Rev. Lett. **109**, 092501 (2012).
[69] J. R. Stone, N. J. Stone, and S. A. Moszkowski, Phys. Rev. C **89**, 044316 (2014).
[70] J. R. Stone, P. A. M. Guichon, P. G. Reinhard, and A. W. Thomas, Phys. Rev. Lett. **116**, 092501 (2016).
[71] C. Fuchs, Prog. Part. Nucl. Phys. **56**, 1 (2006).
[72] G. Shen, C. J. Horowitz, and S. Teige, Phys. Rev. C **82**, 045802 (2010).
[73] C. J. Horowitz and K. Wehrberger, Nucl. Phys. A **531**, 665 (1991).
[74] N. K. Glendenning, *Compact Stars* (Springer, New York, 2000).
[75] S. S. Avancini, D. P. Menezes, M. D. Alloy, J. R. Marinelli, M. M. W. Moraes, and C. Providência, Phys. Rev. C **78**, 015802 (2008).
[76] F. Grill, H. Pais, C. Providência, I. Vidaña, and S. S. Avancini, Phys. Rev. C **90**, 045803 (2014).
[77] M. Dutra, O. Lourenço, and D. P. Menezes, Phys. Rev. C **93**, 025806 (2016).
[78] J. M. Lattimer and A. W. Steiner, Eur. Phys. J. A **50**, 40 (2014).